Multi-Step Cellular Control of Molecular Condensation by Microtubules in Early Oogenesis

Rachael Deis[1,2†], Swastik Kar[1,2†], Adam Ahmad[1,2], Yoel Bogoch[1,2], Avichai Dominitz[1,2], Gal Shvaizer[1,2], Esti Sasson[1,2], Avishag Mytlis[1,2], Ayal Ben-Zvi[1,2], and Yaniv M. Elkouby[1,2*]

[1] Department of Developmental Biology and Cancer Research, The Hebrew University of Jerusalem Faculty of Medicine, Ein-Kerem Campus, Jerusalem, Israel 9112102

[2] Institute for Medical Research – Israel-Canada (IMRIC), Ein-Kerem Campus, Jerusalem, Israel 9112102

[†] Equal contribution

[*] Corresponding author. Email: yaniv.elkouby@mail.huji.ac.il

Abstract

The Balbiani body (Bb) is a membraneless organelle that forms in oocytes from insects to humans. In most vertebrates the Bb contains essential RNA-protein (RNP) granules, establishes oocyte polarity, and is required embryogenesis and reproduction. In mammals the Bb is associated with primordial follicle formation. However, despite its discovery in 1845, the mechanisms of Bb formation are still unknown in any species. Here, we discovered mechanisms of Bb formation in zebrafish. We first provide three lines of live-imaging, molecular, and biochemical evidence in developing ovaries in-vivo to conclude that the Bb forms a molecular condensate. We show that Bb RNPs form insoluble complexes dependently on Buc, an intrinsically disordered protein with a functional prion-like domain, which is essential for Bb formation. By using in vivo live-imaging, FRAP experiments and genetics, we reveal that Bb condensation requires the early liquid-liquid phase-transition of Buc, which later progresses to liquid-solid phase-separation. Further, we uncovered multi-step regulation by microtubules in controlling Bb condensation: first, by direct dynein-mediated trafficking of early condensing Buc granules, then by scaffolding condensed granules likely via molecular crowding, and finally by caging the mature Bb to prevent its over-growth and coarsening, likely by a Pickering effect. These regulatory steps ensure the formation of a single Bb condensate, which is essential for oocyte polarization and development. Our work resolves the origins of embryonic polarity, and identifies molecular condensation as an overlooked phenomena in the developing vertebrate ovary. While phase-separation is often viewed as a self-assembly process, our work proposes a new paradigm for the regulation of molecular condensation widely in biology.

Introduction

Widely in animals and plants, gamete polarization lays the foundations for early embryonic development. However, while vertebrate oocyte polarity has been observed for over two centuries, how it is generated is unknown. The oocyte of most vertebrates, including zebrafish, is polarized along an animal-vegetal axis which is established during oogenesis by a membraneless organelle, called the Balbiani body (Bb)[1-3]. The Bb specifies the oocyte vegetal pole (rev. in[2]), which is critical for embryonic development[1-3]. The Bb contains RNA-protein (RNP) granules of embryonic patterning factors, including dorsal- and germline fate determinants, as well as organelles such as mitochondria[2]. The Bb delivers those RNP granules to the oocyte vegetal pole, from which they later establish the global embryonic body axes and the germline lineage[1-3]. loss of the Bb results in radially symmetrical eggs and early embryonic lethality[4-7].

The Bb is conserved in oocytes from insects to humans[2,5,8-14], where it forms in equivalent stages of oogenesis and exhibits similar dynamics[10,12,13,15]. The human Bb is similar to the zebrafish Bb in morphology and content of organelles, as well as in its cellular and developmental dynamics[13,16,17], but its functions in oogenesis are still unclear because of obvious ethical and technical challenges in the investigation of the prenatal human ovary. In mice, the Bb is associated with proper formation of the primordial follicle[15], suggesting a critical role, but molecular and genetic understanding of the mammalian Bb is lacking. Despite the critical importance of the Bb for oogenesis, embryogenesis, and reproduction, its wide conservation, and its discovery already in 1845[10], mechanisms of Bb formation are still unknown.

We previously characterized Bb formation in zebrafish and identified the oocyte symmetry breaking mechanism that initiates Bb formation at the onset of meiosis[12]. In symmetry-breaking, Bb granules first polarized around the oocyte centrosome by microtubules[12]. After symmetry-breaking, Bb granules continued to aggregate around the centrosome within a nuclear indentation, called the nuclear cleft, and gradually assembled the mature compact Bb[12]. Thus, the Bb develops from a polarized loose aggregate, through gradual assembly into a compact mature compartment (cartoon in Fig. 1A). However, the underlying mechanisms remained unknown. Based on those dynamics, we hypothesized that the Bb could form by a molecular condensation mechanism.

Molecular condensates are increasingly recognized widely in biology (reviewed in[18-22]). Biomolecular condensates are molecular complexes that undergo phase-transition to become less soluble than the remaining cytoplasm[18-22]. The separation of phases in the cell results in de-mixing of the condensed complexes into membraneless compartments with unique content and/or functions. Membraneless condensates are involved in a wide range of cellular processes[18-22], and exhibit different material states that can be placed on a scale from more liquid-like to solid-like[23]. An established example of molecular condensates are RNP granules[24,25], which form in somatic cells[20], or specifically in germ cells and early embryos[19,26].

Condensate phase-transition is mediated by protein regions whose secondary structure cannot be predicted from their sequence, termed intrinsically disordered regions (IDR)[27]. Findings from in-vitro and cell culture studies, as well as from *C. elegans* and *Drosophila* embryos established principles of RNP condensation by IDR interactions[18-22,28-34]. The capability and capacity of IDRs to interact can be modified by shifts in temperature and pH[18-23,35], by RNA binding[25,34,36], and by post-translational modifications[37-39]. These suggest potential cellular regulation. However, the chemical nature of IDR interactions in forming molecular condensates is often described as a self-assembly process (e.g.,[40-43]). The cellular regulatory mechanisms that control phase-separation in vivo, and particularly in vertebrate development and physiology, are poorly understood.

Several observations indicate that the Bb could form by molecular condensation. First, the Bb contains RNP granules, and Bucky ball (Buc), the single known essential protein for Bb formation in any species[4,5], is an intrinsically disordered protein (IDP)[4,44]. Buc also organizes embryonic germ plasm granules in zebrafish, where it was proposed to function equivalently to the Oskar protein, which mediates phase-separation of polar granules in *Drosophila* embryos[45]. Second, the mature Bb in *Xenopus* was described as an inert solid prion-like aggregate that contains amyloid β-sheets[5,46]. Prion-like aggregates are a type of biomolecular condensates[5,47]. However, they are placed at the solid end of the condensation scale[23]. Buc and its *Xenopus* ortholog XVelo contain prion-like domains that were functionally interchangeable in the mature *Xenopus* Bb[5], but the mechanisms of amyloid formation in the mature *Xenopus* Bb, and how it acquire a solid-like states are unknown. These observations suggest that amyloid formation could results from earlier yet unknown Buc condensation dynamics.

Finally, we previously demonstrated genetically that Buc was not required for the initial polarization of Bb granules during symmetry-breaking, but was essential for the subsequent integrity of the aggregate in the cleft[12], suggesting a direct role for the Buc IDP in mediating and/or driving Bb condensation. However, the mechanisms by which the Bb forms during development are unknown and whether it forms by molecular condensation has not been addressed. Furthermore, the dynamics and function of Buc, whether it undergoes phase-separation, and how it is regulated in forming the Bb are unknown.

Here, to test our hypothesis, we investigated the mechanisms of Bb formation, from initial aggregation after symmetry breaking to maturation. We provide live imaging, molecular, genetic, and biochemical evidence in physiological conditions in developing ovaries in vivo, to conclude that the Bb is a molecular condensate. We further reveal that the Bb forms by early liquid-liquid phase-separation and later liquid-solid phase-separation of the Buc protein. We next uncover multi-step regulation over Bb condensation by microtubules: first by dynein-mediated trafficking of condensing granules, then by scaffolding aggregated condensed granules, and finally by caging the mature Bb to prevent its over-growth and coarsening.

Our work resolves mechanisms of Bb formation and the origins of embryonic polarity, which have been elusive for two centuries. Our findings in the developing ovary in vivo, uncover a cellular strategy whereby microtubules orchestrate the cellular control over phase-separation. Considering the vast conservation of the microtubule cytoskeleton, this new paradigm is likely relevant widely in biology. Furthermore, our work identifies molecular condensation as an overlooked phenomena in the developing ovary, shedding new light on female reproduction.

Results

Early dynamic formation of the Balbiany body

The mature Bb in *Xenopus* was described as an inert solid structure that contains amyloid β-sheets[5,46]. However, only isolated late-stage oocytes with mature Bbs were analyzed and the dynamics of Bb formation during earlier stages of oogenesis were not addressed. We previously characterized Bb formation during earlier stages of oogenesis in zebrafish ovaries[12]. Bb formation exhibited developmental dynamics[12] that we hypothesized were consistent with molecular condensation: ***1)*** During symmetry breaking, Buc first localized around the centrosome, increasing its local concentration, ***2)*** Within the cleft, Bb granule aggregation was dependent on the Buc IDP, and ***3)*** The forming aggregate became more compact and appeared denser, finalizing the mature Bb compartment (Fig. 1A). To test this hypothesis, we first aimed to characterize the dynamics of Bb formation, from initial Buc localization after symmetry-breaking to maturation.

We examined Buc dynamics in early oogenesis by both antibody labeling of the endogenous Buc protein in *wt* ovaries, and by live imaging of transgenic Buc-GFP in *Tg(buc:Buc-GFP-buc3'utr)* ovaries[6]. *Tg(buc:Buc-GFP-buc3'utr)* consists of the *buc* genomic locus, and the encoded Buc-GFP protein was shown to accurately recapitulate endogenous Buc protein localization and to be fully functional by rescuing Buc loss of function phenotypes in *buc*$^{-/-}$ fish[6]. Based on our previous characterization of Bb formation in oogenesis[12], we focused on early cleft stages (oocyte diameter of 20-25 μm), mid-cleft stages (oocyte diameter of 30-35 μm), late cleft stages (oocyte diameter of 40-45 μm), and mature Bb stages (oocyte diameter of 50-75 μm) (Fig. 1A). Late cleft and mature Bb stages primarily showed a single localized and large aggregate of either Buc or Buc-GFP (n=34 oocytes in 5 ovaries). In contrast, in early and mid-cleft stages we detected additional smaller granules of Buc and Buc-GFP that did not localize to the main aggregate (n=50 oocytes in 6 ovaries) (Fig. 1A). These observations suggest that the smaller granules in early Bb formation may gradually localize and contribute to the main aggregate, indicating that in contrast with the mature Bb, during development, Buc is more dynamic. We thus sought to test early Buc dynamics in whole developing ovaries.

Live imaging, molecular, and biochemical evidence for Buc dependent Bb condensation

The Bb has been postulated to form by phase-separation (e.g.,[19,26,48]), but definitive evidence to conclude this have not been provided, especially in physiological conditions in vivo. We aimed to unequivocally determine whether the Bb forms by molecular condensation, driven by Buc phase-separation. We followed three lines of investigation, by live-imaging, molecular, and biochemical analyses.

First, to obtain a higher temporal resolution view of Buc dynamics, we performed live time-lapse imaging of Buc-GFP in whole ovaries (Fig. 1B; Movies S1-3). Consistently with our data of Buc and Buc-GFP from fixed ovaries in Fig. 1A, in early and mid-cleft stage oocytes, we detected main Buc-GFP aggregates that localized to the nuclear cleft, as well as smaller non-localized granules (Fig. 1B; Movies S1-3). To analyze the dynamics of early aggregates and granules in three dimensions and over time, we used the IMARIS software to quantitatively track and visualize Buc-GFP intensities in entire Z-stacks of complete oocytes from our whole ovary time-lapse recordings (Fig. 1B; Movies S1-3; Methods). We detected three types of Buc-GFP dynamics (n=25 oocytes, in 5 ovaries): ***1)*** Granules that appeared by increasing their signal intensity, suggesting their condensation in real time (Fig. 1B, top row, white arrowhead; Movie S1), ***2)*** Granules that fused with the main aggregate (Fig. 1B, middle row, white arrowheads; Movie S2), as well as larger aggregates that fused with each other (Fig. 1B, middle row, orange arrowhead; Movie S2), and ***3)*** granules that translocated to the main aggregates and then fused with them (Fig. 1B, bottom row, white and orange arrowheads indicate two examples; Movie S3). These observations of Buc-GFP granules that appear to condense and fuse with each other are consistent with a liquid droplet-like behavior, which is characteristic to dynamic liquid-like molecular condensates[18-22], providing evidence to support Buc phase-separation.

Next, we tested Buc phase-separation molecularly. The small molecule 1,6-Hexanediol is commonly used to specifically interfere with early IDR interactions in multiple molecular condensation processes and prevent their phase-separation[49]. 1,6-Hexanediol (hereafter referred to as Hexanediol) is thought to specifically interfere with reversible early IDR interactions during liquid-liquid phase-separation, while solid-like condensates are less sensitive to treatment with Hexanediol[49]. To test whether Buc complexes in the Bb are sensitive to Hexanediol, we treated whole Buc-GFP ovaries with 5 and 10% Hexanediol and recorded Buc-GFP in live ovaries by imaging Z-stacks every 10 minutes for 90 minutes. To address Buc-GFP sensitivity to Hexanediol during Bb formation we analyzed early cleft, mid-cleft and mature Bb stages (Fig. 1C). Strikingly, we detected dose dependent, as well as stage specific effects of Hexanediol on Buc-GFP. First, smaller Buc-GFP granules in early and mid-cleft stages were most sensitive and were abolished already after 30 minutes (T_{1}) of treatment with 5% Hexanediol (Fig. 1C, top and middle panels, n=63 oocytes, in 8 ovaries). Next, main localized aggregates of Buc-GFP were severely abolished by 5% and 10% Hexanediol treatments after 30 (T_{1}) to 90 minutes (T_{f}) in early cleft stages (Fig. 1C, top panels), but were more mildly affected at mid-cleft stages (Fig 1C, middle panels; n=52 oocytes, in 4 ovaries). Finally, mature Bbs were resistant to both 5 and 10% Hexanediol even after 90 minutes of treatment (Fig 1C, bottom panels; n=56 oocytes, in 7 ovaries). In contrast, in vehicle control ovaries that were cultured and imaged side-by-side to Hexanediol treated ovaries, both the presence of smaller granules and the main aggregates remained intact at all stages and during the entire imaging time, demonstrating that the effects on Buc-GFP in these experiments are specific to treatments with Hexanediol. The specific effects of Hexanediol in early but not late stages oocytes in the same ovary, further provide an internal control to rule out non-specific effects.

We further confirmed the sensitivity of both endogenous Buc protein, as well as the Bb resident *dazl* mRNA to Hexanediol. We reasoned that if Bb RNP granules undergo phase-transition, then the mRNA counterpart of these granules should be affected by Hexanediol as well. The *dazl* mRNA is part of the Bb RNP granule complexes in the mature Bb as well as during all stages of Bb formation in the cleft[2,12]. We thus treated live *wt* ovaries with 5 and 10% Hexanediol, or vehicle control for 90 minutes and then fixed them and co-stained for the Buc protein and the *dazl* mRNA by fluorescent in-situ hybridization (HCR-FISH; Fig. 1D). In contrast to control ovaries, where Buc and *dazl* granules remained intact and both localized to the nuclear cleft in early cleft stage oocytes (n = 4 ovaries; Fig. 1D), both 5 and 10% Hexanediol treatments severely abolished their signals (n = 5 ovaries; Fig. 1D). These results confirm the sensitivity of Buc granule formation and aggregation to Hexanediol, as well as the sensitivity of their *dazl* mRNA counterpart to Hexanediol, consistently with the Buc-GFP data above. The sensitivity to Hexanediol in these experiments strongly suggest that early IDR interactions are required for Buc RNP granule formation during early Bb formation, and further support our hypothesis that Buc undergoes phase-separation.

Finally, we wanted to biochemically determine the solubility state of Buc granules and test whether they constitutes a separate non-soluble phase in physiological conditions. We previously developed a method for a size-based isolation of stage specific oocytes from ovaries[8], which is successfully used for biochemical and omics analyses[44,50]. We first used this method to isolate oocytes at sizes of 50-100 μm in diameter, which represent mature Bb stages, from Buc-GFP transgenic ovaries and confirmed that all oocytes showed a clear signal of Buc-GFP in the mature Bb (Fig. 2A). Next, to examine the solubility of Buc-GFP complexes, we isolated oocytes at all sizes under 100 μm to include all stages of Bb formation. We isolated ovaries collected from three females per sample, lysed them, and centrifuged the lysate to separate the soluble supernatant and insoluble pellet fractions (Fig. 2A). Dissected ovaries, isolated oocytes, and lysates were always kept in zebrafish physiological temperature of 28°C. We next performed western blot analysis on each fraction from lysates to determine in which fractions Buc-GFP is detected (Fig. 2B). Strikingly, Buc-GFP was specifically detected in the non-soluble pellet fraction and not in the soluble supernatant (Fig. 2B, left lane).

To confirm that the presence of Buc-GFP in the pellet fraction resulted from its insolubility, we repeated this experiment and added increasing concentrations of L-Arginine to the lysis buffer. L-Arginine is a solubilizing agent that used to dissolve insoluble complexes[51]. Upon addition of 0.5-1.5M L-Arginine, we detected a dose-dependent increase of Buc-GFP in the soluble supernatant, concomitantly with its decrease from the corresponding non-soluble pellet fractions from the same samples (Fig. 2B). These shifts in Buc-GFP solubility were saturated by 2M L-Arginine. Thus, under physiological conditions, the Buc-GFP protein is part of insoluble complexes that confirm its condensed state in the oocyte.

We next wanted to test whether insoluble Buc-GFP complexes in the pellet fraction represent Bb complexes, and their relevant proteins. We therefore analyzed the pellet and supernatant fractions by mass-spectrometry to determine their protein content. We performed these experiments on oocytes isolated from *wt* and *buc*$^{-/-}$ ovaries. We reasoned that the localization of Bb proteins to the insoluble pellet should be Buc dependent, and anticipated that upon Buc loss of function and the consequent loss of the Bb, Bb-insoluble complexes would be more dissolved. We therefore hypothesized that Bb relevant proteins would be enriched in the pellet over supernatant fractions in the *wt* samples, but not in the pellet fraction of *buc*$^{-/-}$ samples.

We analyzed biological triplicates of each sample and genotype by quantitative mass-spectrometry (Methods). Principle component analysis (PCA) confirmed the clustering of *wt* pellet triplicates, which segregated from separately clustered *wt* supernatant triplicates (Fig. S1A). *buc*$^{-/-}$ supernatant triplicates clustered closer to the *wt* supernatant clusters as expected (Fig. S1A). However, *buc*$^{-/-}$ pellet samples did not cluster with the wt pellet samples, and were more spread, demonstrating that a significant cohort of the *wt* pellet-enriched proteins loose their enrichment in *buc*$^{-/-}$ pellet samples (Fig. S1A). We detected 114 proteins that were specifically enriched in *wt* pellet samples, but not in *buc*$^{-/-}$ pellet samples (Fig. 2C-F; Table S1). Remarkably, *wt* pellet-enriched proteins included proteins that were previously identified from isolated Bbs in zebrafish, including Buc, Zar1, Ybx, Staufen1/2, and Igf2bp3[44] (Fig. 2C-G), validating the presence of Bb relevant complexes in the insoluble *wt* pellet fraction. Strikingly, these proteins were not enriched in the *buc*$^{-/-}$ pellet samples, but were detected at equivalent levels in both *buc*$^{-/-}$ supernatant and pellet samples, demonstrating their shift to the soluble fraction upon loss of Buc function and the Bb (Fig. 2C-G). These results demonstrate that the insoluble state of the enriched proteins depends on the Buc IDP directly, and/or on their association with the Bb.

We addressed the identity and types of the enriched proteins. Gene ontogeny analyses for biological processes, cellular components, and molecular functions revealed that a significantly large portion of the enriched proteins belongs to various RNA biogenesis and processing categories, as well as RNP granules and complexes (Fig. 2H, S1C-D). Thus, we uncovered RNA binding-associated proteins that form insoluble complexes in the oocyte in a Buc-dependent manner. We further examined whether the enriched proteins in our list included IDPs. To predict IDRs in the enriched proteins, we used the PONDR, FoldIndex, and ESpritz algorithms independently (Methods), and found that most of the enriched proteins were predicted to contain IDRs (Fig. 2I, S1B). The enriched proteins that contained the largest IDRs (in percentage of protein sequence) are shown in Fig. S1G, with the IDP Buc and the non-IDP Ziwi proteins as references (Fig. S1E-F).

Similarly, 13% of the enriched proteins were predicted to contain a prion-like domain (PLD), similar to Buc and *Xenopus* XVelo (Fig. 2I). The proteins with the largest PLD (percentage of protein sequence) are shown in Fig. S3, with the PDL Buc and non-PDL Ziwi proteins as references. Altogether, our data identified a list of RNA processing IDPs, some of which including a predicted PLD, that are part of Buc-dependent insoluble complexes. Ultimately, they biochemically demonstrate the insoluble state of Buc and Buc-dependent Bb RNP complexes in vivo.

In summary, three lines of evidence unequivocally conclude the condensed state of Bb granules and the formation of the Bb by Buc phase-separation. First, live time-lapse analysis revealed condensation and fusion of Buc granules, characteristic of condensed liquid droplets (Fig. 1A-B, Movies S1-3). Second, Buc and *dazl* granules were sensitive to IDR interference by Hexanediol (Fig. 1C-D). Lastly, we biochemically determined the insoluble state of Buc-dependent Bb RNP complexes in physiological conditions (Fig. 2A-I, S2-3).

Buc undergoes early liquid-liquid phase-separation and late liquid-solid phase-separation in Bb formation

The liquid-droplet dynamics of Buc (Fig. 1B, Movies S1-3), and the early sensitivity of Buc granules to Hexanediol (Fig. 1C-D), suggest that Buc undergoes early liquid-liquid phase-separation. In addition, the gradually increased resistance of Buc granules to Hexanediol during Bb development and maturation (Fig. 1C), suggest that Buc progresses to undergoing later liquid-solid phase-separation. These dynamics are in line with the detection of prion-like amyloid β-sheets in the mature Bb in *Xenopus*. Prion-like aggregates are amyloid deposits that originally arise from the conformational transition of soluble proteins into highly ordered fibrillar aggregates[52,53]. The prion-like aggregation mechanism ultimately results in the transition of proteins from an initial liquid-like soluble state to a solid-like state[52,53]. Therefore, to test the potential late liquid-solid phase-separation of the zebrafish Bb, we first examined amyloid β-sheet formation in zebrafish oogenesis.

To detect presumptive amyloid β-sheets in live developing ovaries, we used the amyloid β-sheet vital dye ThT, which was used detected amyloid β-sheets in the *Xenopus* Bb[47]. We focused on early Bb formation during cleft stages (oocyte diameter of 25-35 μm) and on the mature Bb (oocyte diameter of 50-75 μm) in Buc-GFP transgenic ovaries. In cleft stage oocytes we only detected background levels of ThT which were not specific to the forming Bb as labeled with Buc-GFP, as well as Bb mitochondria (n=46 oocytes in 4 ovaries) (Fig. 2J). In contrast, in mature Bb stage oocytes, ThT was specifically detected in the Buc-GFP-positive and mitochondria-enriched Bb (n=62 oocyte in 4 ovaries) (Fig. 2J). ThT labeling of the mature Bb was further confirmed in wt ovaries, by Bb co-labeling for endogenous Buc, as well as with the DiOC6 lipid dye that marks the Bb[8,12] (n=73 oocytes in 5 ovaries) (Fig. S3). Thus, similar to *Xenopus*, the zebrafish mature Bb contains presumptive amyloid β-sheets.

Moreover, ThT signals were abolished from mature Bb stage oocytes in *buc*$^{-/-}$ ovaries, where the loss of the Bb was confirmed by either Mitotracker (Fig. 2J), or by co-labeling for Buc and DiOC6 (Fig. S3). In *buc* mutant ovaries, only non-specific background ThT levels were detected in mature Bb stage oocytes (n=51 oocyte in 4 ovaries) (Fig. 2J, S3). These data provide the first genetic evidence for Buc dependent formation of presumptive amyloid β-sheets in the mature Bb, and strongly suggest that amyloid β-sheet formation is part of the final steps of Bb maturation. Overall, these results support our hypothesis that during Bb formation, Buc granules gradually transition from early dynamic liquid-liquid phase-separation, to late Buc-dependent liquid-solid phase-separation and prion-like amyloid formation.

As further validation of these differential developmental dynamics, we next determined Buc turnover during Bb formation. We performed florescent recovery after photobleaching (FRAP) assays in live wholemount Buc-GFP ovaries, measuring Buc-GFP turnover during Bb formation. To address the differential early and late Buc-GFP turnover dynamics, we analyzed early and mid-cleft stage oocytes (diameter of 20-35 µm) and mature Bb stage oocytes (diameter of 50-75µm) (Fig. 3A-E, S4A-C, Movies S4-5). We established adequate bleaching and imaging conditions for consistent bleaching between individual oocytes and different oocyte stages, as well as across experiments (Methods). We bleached an area of approximately 1/3 of the Bb condensate size to ~20% of the original Buc-GFP intensity, and followed recovery for 680 seconds, while imaging every 2.5 seconds. We plotted recovery curves of normalized intensities over time as precent of initial pre-bleach intensity. All individual recovery curves are shown in Supp. Fig. 4A-B. Pooled data is plotted in Fig. 3B as the mean ± SEM for each time point in FRAP recovery curves, at cleft and mature Bb stage oocytes (n=37 cleft stage oocytes in 8 ovaries, and 22 mature Bb stage oocytes in 6 ovaries).

First, we found that after photobleaching, the mature Bb revealed very little recovery, and the bleached area contained almost no Buc-GFP signal (Fig. 3A, red box, Movie S4). This was confirmed by the plotted recovery curves, which only showed ~10% recovery after as long as ~600 seconds (Fig. 3A-B, Fig. S4A, Movie S4). In contrast, at early cleft stages, Buc-GFP showed a much more pronounced recovery to ~40-50% of the initial intensity, within the allotted recovery time (Fig. 3A-B, Fig. S4B, Movie S5). Buc-GFP recovery was faster than during mature Bb stages, and the bleached area gained prominent signal as early as 3 minutes after photobleaching (Fig. 3A-B red box, Fig. S4B, Movie S5). As a control for cell viability and to rule out potential cell damage artifacts in our FRAP experiments, we used the vital dye MitoTracker, which selectively labels live and active mitochondria as a proxy for cell viability. In all our FRAP experiments we co-incubated ovaries with MitoTracker and imaged entire oocytes, including the bleached area, before bleaching and after the 680 seconds of FRAP recording (Fig. S4C). We confirmed that the MitoTracker signal was unaltered in the oocyte, as well as specifically at the bleached area, between the pre-FRAP and the post-FRAP time points (Fig. S4C), validating cell viability, under our experimental conditions.

We next quantified our FRAP results by two methods. First, we followed the immobile/mobile fraction analysis method[54-56]. In this method, the immobile fraction is defined as the incomplete recovery observed at the site of bleaching due to some fraction of the molecules that are immobilized, and the mobile fraction is defined as the rest of the molecules that contribute to the fluorescence recovery. We calculated the immobile and mobile fractions of Buc-GFP. Mobile fractions in cleft stage oocytes were 44.88 ± 14.29%, and only 12.57 ± 3.86% at mature Bb stages (Fig. 3C-E). Concomitantly, immobile fractions were 55.11 ± 14.29% at cleft stages and as high as 87.42 ± 3.86% at mature Bb stages (Fig. 3C-E). As a second quantification, we plotted at each oocyte stage, the relative Buc-GFP signal intensity during the last 20 frames of our 680 seconds recording post-bleaching. The relative intensity was 0.49 ± 0.14 at cleft stages, but only 0.15 ± 0.03 at mature Bb stages, further confirming the higher early recovery (Fig. 3C-E).

Early Buc-GFP recovery in these experiments occurred over the course of minutes, which is a little slower than the recovery over seconds that is typically reported for condensate proteins. This could results from biological and/or technical reasons: ***1)*** The microscopy optics are different between our in-vivo settings in the intact organ and in-vitro solutions or cell monolayers which are typically used in FRAP measurements. ***2)*** In our experiments, Buc-GFP is expressed at functional levels from its endogenous promoter, and thus likely at physiological levels. In in-vitro or cell culture FRAP experiments, proteins are often used in high non-physiological concentrations, or are over-expressed, which could affect recovery dynamic and/or regulation. ***3)*** The time-scale of molecular condensation dynamics could vary in a cell- and tissue-specific manner. For example, differences exist between the timeframes of stress granule formation in response to stress, P granule dynamics in the first divisions of the developing *C. elegans* embryos, and the prolonged formation of the Bb in oogenesis. Differential time scales of condensation might have been overlooked by the shortage in studies of condensates in physiological systems in vivo.

Altogether, the above experiments confirm the stable solid-like nature of the mature Bb as was shown in *Xenopus*[5,46], and demonstrate that during earlier stages, Buc exhibit higher turnover rates, which are consistent with its liquid-like state. We conclude that the Bb undergoes a gradual condensation process, as follows: ***1)*** initially, Buc drives the liquid-liquid phase-transition of small Bb RNP granules, ***2)*** during early-mid Bb formation, Buc and small Buc phase-separated granules are dynamic and are continuously supplied to the growing main condensate and fuse with it, ***3)*** In the main condensate, Buc continues to drive the condensation of Bb granules, which results in formation of amyloid β-sheets and liquid-solid phase-transition, ***4)*** ultimately, the solid-like state of Bb granules finalizes the typically dense, stable, and compact morphology of the mature Bb.

Microtubules are required for Buc granule turnover in the early forming Bb condensate

The rate and cellular localization of molecular condensation can be critical for function in physiological and developmental systems. In oocyte polarity, the formation of a single localized Bb condensate is critical. In *buc*$^{-/-}$ oocytes, Bb mRNAs are not localized but are randomly distributed in the oocyte cytoplasm, failing to specify the distinct animal and vegetal poles of the oocyte and resulting in radial eggs and embryos, and consequent embryonic lethality[7]. Thus, randomly distributed condensed Buc RNP granules would be detrimental to oocyte polarity and embryogenesis. To form functional eggs, condensed Buc granules must be localized. Therefore, we asked what regulates Buc turnover in condensing granules and how they are localized to the main condensate.

Considering the role of microtubules in Bb granule localization during the preceding symmetry breaking stages[12], we reasoned that microtubules are strong candidate regulators of condensing Buc granules in the cleft. Furthermore, we previously detected the presence of microtubules around the centrosome in the nuclear cleft, as detected in *Tg(βAct:EMTB-3GFP)* transgenic ovaries[12]. Here, using improved imaging conditions which successfully resolves EMTB-GFP labeled microtubule cables in developing ovaries, we characterized the organization of microtubules in cleft- and mature Bb stage oocytes (n=15 ovaries) (Fig. 3F). In early cleft stages, we detected microtubule cables generally in the cytoplasm, as well as a prominent meshwork of microtubule cables specifically in the nuclear cleft (Fig. 3F, top left panel). In mid-late cleft stages, microtubule cables extended more generally in the cytoplasm and retracted from a region that appeared like the presumptive Bb aggregate (Fig. 3F, top middle panel). In mature Bb stages, the network of microtubule cables was more elaborated generally in the cytoplasm, and they now formed a cage-like organization around a region they were retracted from, which appeared like the presumptive mature Bb compartment (Fig. 3F, top right panel). We validated these microtubule organization dynamics by live imaging of EMTB-GFP ovaries (n=20 ovaries) (Fig. 3F, bottom panels), confirming that these dynamics represent the native organization of microtubules in oogenesis and do not result from fixation conditions.

To test whether the above microtubule dynamics overlap with Buc dynamics in the forming Bb, we co-labeled ovaries for microtubules and Buc (n=6 ovaries) (Fig. 3G). In mid-late cleft, as well as mature Bb stage oocytes, Buc localized to a region from which microtubules were retracted, consistently with the detection of microtubules above (Fig. 3F). However, in early cleft stages, Buc granules and the microtubule meshwork both localized to the cleft and strikingly, individual microtubule cables appeared to be interwoven through Buc granules (Fig. 3G). dSTORM super-resolution microscopy of ovaries co-labeled for EMTB-GFP and Buc, confirmed this co-organization of Buc granules and microtubules, and detected Buc granules that were intimately adjacent to microtubule cables in the cleft (n=4 ovaries) (Fig. 3H, S4D). Therefore, the organization of a microtubule meshwork specifically in the cleft, corelates developmentally with the stages of high Buc turnover, demonstrating that microtubules are positioned correctly in both time and space to control Buc dynamics. Furthermore, the intimate proximity of Buc granules to individual microtubule cables suggests that microtubules could transport condensing Buc granules via a trafficking mechanism.

To test the roles of microtubules in mediating early Buc turnover, we performed FRAP experiments in Buc-GFP ovaries upon treatments with two different microtubule depolymerizing drugs, nocodazole and colchicine, as well as DMSO as control (Fig. 4 A-J, S5, Movies S6-7). We first confirmed the depolymerization of microtubules in our treatment conditions, by monitoring EMTB-GFP signals in treated ovaries (Fig. S5G-H). DMSO treated ovaries exhibited clear and normal EMTB-GFP-positive microtubule cables in oocytes, while both nocodazole and colchicine treatments resulted in their depolymerization, as depicted by diffused EMTB-GFP signal (Fig. S5G-H). Next, we performed FRAP experiments in early and mid-cleft stage oocytes (diameter of 20-35 µm) as in Figure 3. DMSO treated ovaries exhibited Buc-GFP recovery curves that reached ~40-50% recovery (n=17 oocytes), consistently with Buc-GFP recovery curves in non-treated ovaries in Fig. 3 (Fig. 4 A-J, S5, Movies S6-7). In contrast, in conditions where microtubules were depolymerized by either treatment with nocodazole (n=20 oocytes) or colchicine (n=14 oocytes), Buc-GFP recovery was abolished and only reached ~10-15% recovery (Fig. 4 A-J, S5, Movies S6-7). FRAP quantification by calculating the mobile/immobile Buc GFP fractions, as well as by measuring intensities in the last 20 frames, confirmed the normal recovery in the DMSO control treated ovaries, and the abolished recovery upon microtubule depolymerization by nocodazole and colchicine (Fig. 4C-E, H-J).

As a control for the effect of nocodazole and colchicine on microtubules, we repeated these experiments in Buc-GFP ovaries upon treatment with the microtubule stabilizing drug Taxol, where we confirmed that microtubules are not depolymerized (Fig. 4 K-O, Supp. Fig. 5E-F, I, Movie S8). As shown by FRAP images (Fig. 4 K-O, Movie S8), recovery plots (Fig. 4L, S5E-F), and quantifications (Fig. 4 M-O), Buc-GFP exhibited normal recovery in Taxol treated ovaries (n=17 oocytes), similar to its recovery in control DMSO treated ovaries (n=14 oocytes) and in non-treated ovaries (Fig. 3). Notably, the overall recovery in Taxol treated ovaries was slightly higher than in DMSO control treated ovaries (Fig. 4L, O), upon microtubule stabilization. Furthermore, cell viability as measured by Mitotracker signals before and after FRAP was not affected by either drug treatment (Fig. S5J-L). We conclude that microtubules are required for Buc-GFP recovery, and thus its turnover in the early forming Bb.

Dynein-mediated trafficking of condensing Buc granules is required for Buc granule turnover in the early forming Bb condensate

The requirement of microtubules for Buc turnover (Fig. 4) and the tight proximity of Buc granules to individual microtubule cables as shown by our super-resolution microscopy data (Fig. 3H), suggest that microtubules could transport Buc granules via a trafficking mechanism. Buc granules localize towards the centrosome, which is located in the vicinity of the cleft and its organized microtubule meshwork[12]. Thus, granule trafficking would be directed towards the centrosome (-)end of microtubules and likely to be executed by the dynein (-)end motor protein. To test the roles of dynein in Buc turnover, we repeated the above FRAP experiments in Buc-GFP ovaries upon treatment with either DMSO control, or the dynein inhibitor ciliobrevin (Fig. 5A-E, S6A-B, Movie S9). We previously established conditions for validated inhibition of dynein by ciliobrevin in cultured ovaries[57]. In contrast with DMSO control treated ovaries, which exhibited normal ~40% Buc-GFP recovery (n=20), ciliobrevin treatment abolished Buc-GFP recovery to ~10% (n=15) (Fig. 5A-E, S6A-B, Movie S9), similar to the effects of microtubule depolymerization (Fig. 4). FRAP quantification confirmed these results (Fig. 5C-E, S6A-B), concluding that dynein activity is required for Buc turnover in early Bb formation.

Notably, dynein can anchor microtubules to various cellular structures and thus may affect microtubule organization and/or stabilization[58]. We wanted to determine whether in the forming Bb, dynein is required directly by trafficking Buc granules, or indirectly by organizing microtubules in the cleft. We first examined the general organization of microtubules in ovaries upon ciliobrevin treatments and found that they were indistinguishable from their organization in DMSO treated or non-treated ovaries (Fig. S4E). This indicates that dynein is not essential for microtubule organization at these stages, and supports a direct role for dynein in trafficking Buc granules.

To functionally test this, we repeated the above FRAP experiments, but this time added Taxol to the cultured ovaries prior to the addition of ciliobrevin (Fig. 5F-J, S6C-D, Movie S10). We reasoned that if dynein indirectly organizes and/or stabilizes microtubules, then priming microtubule stabilization by Taxol should prevent their disorganization and rescue Buc-GFP turnover upon ciliobrevin treatment. In contrast, if despite microtubule stabilization Buc-GFP turnover is still abolished by dynein inhibition, this would suggest a direct trafficking mechanism. The general organization of microtubules in ovaries co-treated with Taxol and ciliobrevin was indeed indistinguishable from their organization in DMSO treated or non-treated ovaries (Fig. S6G). In FRAP experiments, DMSO treated (n=10), and Taxol treated ovaries (n=12), showed normal ~40% recovery, consistently with non-treated ovaries (Fig. 3), and our experiments above (Fig. 4-5). However, in ovaries treated with both Taxol and ciliobrevin (n=15), Buc-GFP recovery was abolished to around 15%, phenocopying the effects of ciliobrevin alone, failing to rescue recovery (Fig. 5F-J, S6D, Movie S10), and arguing for a direct role of dynein in Buc granule trafficking. Oocyte viability was not affected in all the above FRAP experiments, as shown by Mitotracker live co-labeling (Fig. S6H-I).

Further supporting a direct trafficking mechanism, we found that dynein co-localizes with Buc in early cleft stage oocytes, as shown by co-labeling ovaries for Buc and dynein (Fig. 5K-L). Considering the multiple roles of dynein in cells, puncta of dynein signals were distributed in the oocyte cytoplasm as expected (Fig. 5K). However, we detected pronounced puncta in the cleft that appeared to co-localize with Buc granules (Fig. 5K). Statistical pixelwise colocalization analysis (Methods) in the cleft regions of interest (ROI) from 31 oocytes, showed Pearson's R values of 0.665 ± 0.16 (Fig. 5L), which concludes that dynein puncta in the cleft co-localize with Buc granules.

To unequivocally conclude Buc granule transport by dynein mediated trafficking, we biochemically tested whether Buc and dynein form common protein complexes in developing oocytes at the relevant stages of Bb formation. To identify Buc binding proteins, we isolated all oocytes smaller than 100 μm in diameter from Buc-GFP ovaries, as in Figure 2, and performed immune-precipitation (IP) experiments using Buc-GFP as bait with GFP dynabeads, followed by mass-spectrometry analysis (Fig. 5M-O, S7). We used three independent controls in our analyses: ***1)*** To control for bead nanobody specificity, we compared Buc-GFP IP samples with control beads (no GFP nanobody) IP (Fig. 5 M, S7C), ***2)*** To control for Buc IP specificity, we compared Buc-GFP IP with IP samples from *wt* ovaries that do not express GFP (Fig. 5N, S7C), as well as ***3)*** with GFP IP samples from a transgenic line driving free cytoplasmic GFP in the germline [*Tg(vasa:GFP)*[59]] (Fig. 5 O, S7C). We first confirmed successful and specific IP of Buc-GFP by western blot (Fig. S7A), as well as the successful and specific IP of proteins in Buc-GFP IP samples, by silver-stain analysis (Fig. S7B). Quantitative mass-spectrometry analysis identified 90 proteins that are specifically enriched in Buc-GFP IP over the three independent control IP samples (Fig. 5M-O, S7C-D, Table S2). Enriched proteins included known Bb proteins, proteins of known Bb resident transcripts, and the Buc protein (Fig. 5M-O, S7C-D). Strikingly, the cytoplasmic dynein light chain subunits, dynein light chain LC8-type 1 (Dynll1) and dynein light chain LC8-type 2b (Dynll2b), were specifically enriched in Buc-GFP IP samples (Fig. 5M-O, S7C-D). Dynein light chains LC8-type 1 and 2 are accessory components of the cytoplasmic dynein complex that are thought to be involved in linking dynein to cargos and to adapter proteins that regulate dynein function[60]. Thus, these results confirm the binding between Buc and the cytoplasmic dynein complex.

Importantly, Buc-GFP-IP enriched proteins included known Bb proteins (such as Igf2bp3), as well as proteins involved in mammalian oocytes RNA storage bodies called MARDO[61], such as Zar1, Ybx1, 4E-T, LSM14, and DDX6[61] (Fig. S7C, Tables S2). Consistently with our detection of Buc-dependent insoluble Bb complex protein by mass-spectrometry in Fig. 2, gene ontogeny analyses for biological processes, cellular components, and molecular functions revealed that a significantly large portion of the enriched proteins belonged to various RNA biogenesis and processing categories, as well as RNP granules and complexes (Fig. S7E). Furthermore, enriched proteins included many that had IDRs (Fig. S8), as well as a PLD (Fig.

S9). Thus, the enriched proteins from our Buc-GFP-IP dataset are in general consistent with the proteins we identified in Buc-dependent insoluble Bb complexes (Fig. 2).

We further validated the Buc-dynein protein-protein interaction in IP experiments followed by dot blot analysis. Cytoplasmic dynein complexes are composed of varying light chain isoforms and a common heavy chain protein[60]. We therefore used an available antibody for dynein heavy chain that was confirmed to work well in zebrafish[62]. Considering the extremely large size of dynein heavy chain (~500 KD), detecting this protein in a gel by western blot analysis would be highly challenging if at all feasible. We thus performed IP in all Buc-GFP and control samples as above, detecting the dynein heavy chain subunit by dot blot analysis (Fig. 5P, S10). We confirmed the successful and specific IP of GFP in Buc-GFP and free GFP samples, but not *wt* IP or control bead samples (Fig. 5P, S10C). We also confirmed the detection of dynein heavy chain in all input samples (Fig. 5P, S10B). In contrast, in IP samples, dynein heavy chain was specifically detected in Buc-GFP IP, but not free GFP or any other IP control (Fig. 5, S10A). As a loading control, we detected β-act in all input samples (Fig. 5P, S10D). β-act was not detected in Buc-GFP IP with dynein heavy chain, confirming the specificity of dynein heavy chain IP (Fig. 5P). Fig. S10 shows different exposures of the raw blots for both input and IP samples of the representative experiment in Fig. 5P.

Altogether, our work provides thee lines of evidence to conclude that the dynein motor complex transports condensing Buc granules on microtubules in early Bb formation: ***1)*** Condensing Buc granules localize adjacent to microtubule cables (Fig. 3) and co-localize with dynein in the cleft (Fig. 5), substantiating their correct spatial-temporal interaction as expected from trafficked complexes, ***2)*** Microtubules and dynein activity are required for Buc-GFP turnover in the forming Bb condensate in the cleft (Fig. 4-5), providing functional proof for their mediated transport, ***3)*** The Buc protein forms complexes with the dynein heavy chain, as well as the Dynll1 and Dynll2b light chain subunits (Fig. 5), which together very likely represent a dynein transport complex, providing biochemical proof for their association. Furthermore, Buc is the single known essential protein for Bb formation. Our IP experiments provide an important list of promising new candidate Buc interacting proteins that could uncover upstream regulators, partners, or downstream targets of Buc for future investigation of Bb condensation mechanisms, as we did here for the dynein complex.

A microtubule meshwork scaffolds the main Buc condensate

Having established microtubule functions in controlling early condensing Buc granules, we next wanted to examine whether they play additional roles in controlling already condensed granules in the main aggregated Bb condensate in the cleft. We sought to evaluate the localization and integrity of the main Bb condensate upon microtubule depolymerization by nocodazole treatments after the formation of the condensate (Fig. 6A). From our extensive image analyses in live and fixed data in this work and throughout our characterization of early oogenesis in zebrafish (e.g.,[8,12,57]), we empirically determined that the progression through developmental stages in oogenesis, as well as formation of the nuclear cleft and the Bb condensate in it, are much more prolonged than the 90 minute time-course of our treatments. Thus, oocytes with detectable nuclear clefts at the end of our treatments, have already formed the Buc condensate prior to treatment. This allowed us to directly address the effects of microtubule depolymerization on Buc granules, specifically after their condensation in the cleft.

We treated live Buc-GFP ovaries with nocodazole and fixed them for Buc-GFP immune-staining. We co-stained for Buc-GFP and separately two landmarks for the cleft and the Bb aggregate: mAb414, which labels nuclear pore complexes on the nuclear envelop delineating the nuclear cleft (Fig. 6A, S12), and γTub marking the centrosome in the vicinity of the cleft[12] (Fig. 6A). In DMSO control treated ovaries, Buc granules were normally localized in an intact condensate within the cleft in 78.5±4.95% of oocytes at cleft stages (oocyte diameter of 20-25μm), with 21±4.95% showing abnormal dispersed or expanded granules (n=126 oocytes from 6 ovaries; Fig. 6A-B). In contrast, in nocodazole treated ovaries, Buc granules were normally localized in an intact condensate in only 45.69±11.24%, but dispersed and expanded in 54.31±11.24% of clef stage oocytes (n=163 oocytes from 6 ovaries; Fig. 6A-B), demonstrating that the main Buc condensate disintegrates upon microtubule depolymerization.

We quantified these phenotypes by two methodologies. We first measured the intensities of Buc in the nuclear cleft in partial z-projection images. We generated partial z-projection images of oocytes around the plane in which the cleft was most pronounced, and in which the centrosome was located (Fig. 6C, top). In a second set of experiments, we identified this region of the cleft based on mAb414 nuclear envelop labeling (Fig. 6C, bottom, Fig. S12A, E). We then drew a 9 μm line across the cleft opening (Methods; Fig. 6C S12A, E), and measured Buc intensities along this measuring line. We normalized Buc intensities (Methods) and plotted them along the measuring line position (Fig. 6E). Fig. 6D-K shows pooled data from two representative experiments, whose individual row data are shown in Fig. S11 (experiments #1 and #2 in Fig. S11A-G, and H-N, respectively).

In DMSO control and nocodazole treated ovaries, we generally detected two types of Buc intensity plots across oocytes. In type-I, normalized Buc intensities showed a curve with a clear peak (blue curves in Fig. 6E-F, S11C, G, J, N, raw curves in Fig. S11A, D, H, K), representing the prominent Buc condensate. In type-II, normalized Buc intensities appeared flattened and were defined as curves whose maximal normalized intensity was lower than 25% of the maximal type-I intensity (red curves in Fig. 6E, S11F, G, J, N, raw curves in Fig. S6 B, E, I L), likely representing disintegrating Buc condensates. We pooled all curves from each condition and plotted the mean ± SD values of normalized intensities per position along the measuring line. Fig. 6E shows pooled data of curve types in DMSO-control treated ovaries, and Fig. 6F shows pooled data for curve types in nocodazole treated ovaries. As shown in Fig. 6D, in DMSO control treated ovaries, 99±1.41% of oocytes showed type-I curves, and only 1±1.41% showed type-II curves (n=87 oocytes from 6 ovaries; Fig. 6D). In contrast, in nocodazole treated ovaries, only 64.65±18.88% of oocytes showed type-I curves and 35.35±18.88% showed type-II curves (n=112 oocytes from 6 ovaries; Fig. 6D).

To evaluate the effects of microtubule depolymerization on Buc condensate integrity, we compared the flattened type II curves from oocytes in nocodazole treated ovaries (red, Fig. 6F) with the normal type-I curves in oocytes from control DMSO treated ovaries(blue, Fig. 6E) in Fig. 6H. The differences between those curves were statistically significant (Fig. 6H). The *P*-values from Fig. 6H are plotted in Fig. 6I, showing the lowest *P*-values around the center of the measuring line and reflecting the dispersal of Buc granules from the normal prominent Buc condensate upon microtubule depolymerization.

We further found that the curvature of type-I-like curves in oocytes from nocodazole treated ovaries (Fig. 6F, purple curves) appeared more dampened than the curvature of type-I curves in control oocytes (Fig. 6E, blue curves). Those differences in curve peaks between type-I curves from control ovaries (blue, Fig. 6E) and type-I-like curves from nocodazole treated ovaries (purple, Fig. 6F), were statistically significant (Fig. 6G). We therefore defined the purple type-I-like curves in nocodazole treated ovaries as type-III. This revealed that even oocytes that we considered to exhibit normal curves in Fig. 6D (blue), were mildly affected, showing reduced intensity of the Buc condensate upon microtubule depolymerization, and further indicating Buc dispersal.

Validating these analyses, consistent results were obtained from identical experiments in ovaries co-labeled for Buc and mAb414 (instead of γTub for centrosome), as shown in Fig. S12. Line measurements (Fig. S12A, E), raw type I and type II curves (Fig. S12B-C, F-G), and pooled data curves (Fig. S12D, H), confirmed Buc condensate disintegration upon microtubule depolymerization (Fig. S12I-J), when using mAb414 signals as a second cleft landmark in our analyses.

As a second quantification, we analyzed these Buc condensate phenotypes upon microtubule depolymerization in three-dimensions (3D) throughout entire oocyte Z-stacks. We analyzed the entire volume of oocytes that were co-labeled for Buc-GFP and γTub from the above experiments, by using the IMARIS software (Fig. 6J, Movies S11-12). To confirm the above phenotypes in 3D, we analyzed representative control oocytes with normal Bb condensate, and nocodazole treated oocytes with expanded and dispersed granules (Fig. 6J, Movies S11-12). Oocytes from control DMSO treated ovaries showed a clear prominent Buc condensate in 3D that was adjacent to the centrosome (n=16 oocytes; Fig. 6J, left, Movies S11-12, top). In contrast, nocodazole treated oocytes with dispersed and expanded granules showed multiple smaller aggregates in 3D (n=14 oocytes; Fig. 6J, right, Movies S11-12, bottom).

3D quantification in IMARIS showed that upon microtubule depolymerization, the total number of aggregates per oocytes was increased (Fig. 6K). Specifically, the number of smaller aggregates per oocyte was increased. The number of smaller aggregates by surface area ($<5\mu m^2$) per oocyte was increased (Fig. 6L). Consistently, the number of smaller aggregates by volume ($<5\mu m^3$ in Fig. 6M, or $<1\mu m^3$ in Fig. S13A) per oocyte was increased as well. Furthermore, the distance between detected aggregates to the centrosome was increased upon microtubule depolymerization. The distances of all aggregates from the centrosome per individual oocytes are plotted in Fig. S13B, and the average aggregate-centrosome distance from all oocytes in each condition are plotted in Fig. 6N. Both plots show a clear increase in distances. Altogether, the detection of more numerous aggregates that were smaller and more distant from the centrosome, essentially demonstrate the disintegration of the Buc condensate under these conditions.

In sum, our data conclude that that the microtubule meshwork, which is interwoven with the Buc condensate in the cleft, (Fig. 3), is required to physically scaffold Buc granules, after their delivery to the cleft, by two non-mutually exclusive mechanisms: ***1)*** Microtubules could contribute to maintaining Buc granules in close proximity to facilitate and support their fusion (as demonstrated in Fig. 1A-B, Movies S2-3), since upon microtubule loss, the Bb condensate disintegrates to smaller distant granules (Fig. 6A-F, red curves, and Fig. 6 J-N), ***2)*** Microtubules could contribute to keeping local Buc concentrations sufficiently high to maintain granule condensation, since upon microtubule depolymerization Buc dissolves from the condensate (purple dampened intensity curves in Fig. 6F-G).

Microtubules form a cage-like organization around the mature Bb to prevent its over-growth and coarsening

As shown in figure 3, later in development, microtubule cables were absent from the vicinity of the mature Bb, but spanned around it, forming a cage-like organization. Having establishing that microtubules are required for trafficking condensing Buc granules to the main Bb forming Buc condensate, and then for maintaining its integrity, we sought to examine potential later roles of microtubules in controlling the mature Bb.

To test the roles of microtubules in potentially contributing to the organization of the mature Bb, we examined Buc-GFP oocytes at mature Bb stages (oocyte diameters of 50-100 μm). Whole early developing ovaries are thin and ideal for microscopy as shown by our analyses thus far, but they contain fewer oocytes at mature Bb stages. On the other hand, later developing ovaries are abundant with mature Bb oocytes, but two technical challenges prevent their high quality quantitative imaging. First, these ovaries are thicker and opaque, and second, mature Bb oocytes are scattered at different Z positions and deep in the tissue. These challenges reduce the quality of image acquisition, especially by live time-lapse imaging, and requires demanding identification and imaging of individual oocytes. To perform quantitative image analyses on oocytes at these stages and in high numbers, we analyzed isolated oocytes in short-term culture. Isolated oocytes at these stages remain normally vital and continue to develop for at least 24 hours in culture[63]. Here, we cultured oocyte for a total of 150 min throughout our experiments below. To culture oocytes, we isolated them form adult ovaries, where they are abundant (Fig. 2A), using our isolation protocol[8,50], as also described above (Fig. 2A).

We isolated mature Bb oocytes at sizes ranging between 50-100 μm in diameter from Buc-GFP ovaries and mounted them in a single layer on a glass-bottom dish, embedded in low-melt agarose and culture media (Methods). We cultured isolated Buc-GFP oocytes, treated them with nocodazole or DMSO as control, and monitored the Buc-GFP-positive Bb over time. In these settings, where all oocytes are aligned approximately on a single Z plane, we could efficiently image many oocytes simultaneously. In each experiment, we monitored microtubules depolymerization in oocytes that were isolated form the EMTB-GFP line and cultured side by side to the Buc-GFP oocytes. Microtubules were depolymerized after ~60 min in this assay (Fig. S14A), and we started recording Buc-GFP oocytes from this time point (set as T_0). We monitored the Bb by imaging entire oocytes every 1 min, for 90 min (set as T_F). MitoTracker labeling confirmed the viability of oocytes through the course of our experiments.

We segmented the entire volume of oocytes and the Bb throughout the course of those live recordings using the IMARIS software. 3-dimensional segmentations of the Bb in control DMSO treated oocytes, showed that the size of the Bb was unaltered, with only slight fluctuations (Fig. 7A-B, Movie S13), consistently with the stable nature of the solid-like mature condensate. In contrast, we found that upon nocodazole treatment, the Bb became inflated and grew amorphic protrusions over time (Fig. A-B, Movie S13). As control, the total volume of oocytes was confirmed to remain unaltered in both DMSO and nocodazole treatments throughout the experiment (Fig. 7C, bottom right).

To analyze this phenotype, we used IMARIS to measure and track the volume and surface area of the Bb over time in control-DMSO and nocodazole treated oocytes (Fig 7C, S14B). To normalize for Buc-GFP expression levels we normalized the Buc-GFP signal in the Bb to its background levels in the remaining cytoplasm per oocyte. To control for oocyte size and potential minor developmental stage variability, we segmented the entire oocyte volume and surface area, and normalized the values of the Bb to those of their corresponding oocytes at each time point. We then plotted the fold-change in Bb volume and surface area in each time point relative to their corresponding values at T_0 per oocyte and over time (Fig. 7C, S14B). Fig. S14 shows three representative experiments, for each of which, plots of pooled data from all oocytes per experiment are shown for each parameters (in each experiment oocytes were collected from ovaries from two fish). The pooled data (mean ± SD) from all three experiments and for all parameters are plotted in Fig.7 B.

Our 3-dimensional measurements first confirmed the constant size of oocytes over the course of our experiments (Fig. 7B, S14B). They further confirmed that in control DMSO treated oocytes, the size of the Bb, as measured by both volume and surface area is unaltered throughout our experiments (Fig. 7C, S14B). Strikingly, in nocodazole treated oocytes, we measured a 2.6 ± 0.44 -fold increase in Bb volume, and 2.16 ± 0.23 -fold increase in Bb surface area over 90 minutes (Fig. 7C, S14B). These results demonstrate that microtubules are required for maintaining the morphology and confining the size of the mature Bb. Previous work attempted to test the role of microtubules in controlling the mature Bb and found that the mature condensate is not degraded upon microtubule depolymerization by nocodazole treatments[46,63]. However, these experiments did not examine Bb dynamics over time, but analyzed snapshots of oocytes.

Moreover, they were focused on potential degradation of the Bb, and did not address a potential increase in Bb size.

The increase in the size of the Bb could potentially result from an accelerated supply of new Buc-GFP molecules to the Bb over the normal rate of Buc-GFP turnover, for unknown reasons upon microtubule depolymerization. We measured the density of the Buc-GFP signal in the Bb over time, reasoning that if the Bb grows due to an accelerated supply of Buc-GFP, its signal density should not decrease during growth. We found that Bb density decreased with Bb growth to 69.66 ± 7.09 % of density at T_0 (Fig. 7C, S14B). These results preclude that an acceleration in Buc-GFP supply is a major cause for the increase in the size of the Bb, consistently with the low turnover of Buc-GFP in the mature Bb as measured in our FRAP analyses (Fig. 3).

The increase in the size of the Bb which appears as an inflation or bloating of the Bb with growing amorphic protrusions, may be consistent with an Ostwald ripening phenomenon, which drives the growth and coarsening of condensates[49,64]. Ostwald ripening occurs because larger condensates are energetically favored over smaller ones, since IDR interactions at their surface are less stable[49,64]. The low turnover of Buc at these stages is likely sufficient to facilitate Ostwald ripening during the slow coarsening over 90 minutes that we observe. It remains to be determined if other possible physical mechanisms that were shown in theoretical an/or in vitro models, may contribute to the growth of the Bb and its protrusions in addition to Ostwald ripening (e.g.,[65-67]).

In either way, previous genetic studies showed that the size of the Bb must be controlled. Loss-of-function mutations in the Microtubule-Actin Crosslinking Factor 1 (Macf1) protein, which mediates cytoskeletal interactions, resulted in an enlarged Bb (for previously not understood reasons) and prevented its proper docking to the oocyte cortex[63]. Consequently, oocytes failed to polarize, resulting in infertility[63]. Thus, an oversized and coarsened Bb is likely non-functional, highlighting the need for its control by microtubules as we show here.

Discussion

Our work uncovered mechanisms controlling molecular condensation in a post-embryonic developmental vertebrate system in-vivo. We demonstrate that the Bb meets all criteria of molecular condensates, as follows: ***1)*** We establish that early granules of the Buc IDR are liquid-like, exchange Buc with the dilute phase, translocate and fuse, and are sensitive to early IDR interference by Hexanediol. ***2)*** We established that the later condensate hardens to a sloid-like state, exhibit low exchange of Buc with the dilute phase, is resistant to Hexanediol, and forms Buc-dependent presumptive amyloid structures. ***3)*** We provide strong biochemical evidence that conclude that the Bb contains Buc-dependent insoluble RNP complexes in oocytes at the correct developmental stages. Based on this evidence we conclude that the Bb forms by early dynamic liquid-liquid phase-separation of Buc, and then its liquid-solid phase-separation during the maturation of the compact stable Bb (Fig. 7D).

The precise mechanisms underlying the maturation from liquid-liquid to liquid-solid phase separation are still unclear. They presumably involve increasing saturation of Buc IDR interactions as generally suggested[68,69], and possibly combined with yet unknown activity via Buc PLD. Buc PLD is likely functional since it was shown to be interchangeable with XVelo PLD in the mature *Xenopus* Bb[5]. Consistently with this, in Drosophila oocytes, the maturation of *oskar* RNA granules from liquid-liquid to liquid-solid phase separation, required the PLD domain of the *oskar*-binding protein Bruno[32]. Those IDR interactions and/or PLD activity, are likely regulated by post-translational modifications of Buc. Our lists of candidate Buc interacting proteins now provides a stepping stone to uncover their function in potentially regulating Buc in future investigation.

We further deciphered mechanisms for the multi-step regulation by microtubules in controlling Bb condensation (Fig. 7D). First, we demonstrate direct dynein-mediated microtubule trafficking of early condensing Buc granules. Dynein-mediated trafficking supplies Buc granules to the main forming Bb condensate and is required for Buc turnover (Fig. 7D, left). Second, we show that in the main condensate, microtubules are essential to likely physically scaffold condensed granules. The microtubule meshwork in the cleft is required to prevent condensate disintegration to smaller granules, as well as to prevent Buc dissolution from the condensate (Fig. 7D, middle). These observations suggest that microtubules potentially serve as molecular crowding agents that keep granules in close proximity to support their fusion, and maintain Buc at sufficient concentration to support its condensation. These findings in vivo are supported by in vitro TIRF assays, in which the presence of microtubules could replace the need for the crowding agent polyethylene glycol (PEG) for the condensation of the Cobl protein[70].

Finally, we demonstrate that microtubules cage the mature Bb to prevent its over-growth and coarsening. Condensate coarsening can be controlled by a Pickering effect, whereby solid particles that absorb on the surface of an emulsion (condensate), between the emulsion and its more soluble surrounding, stabilize the emulsion[71]. A Pickering effect was demonstrated to act in physiological conditions in *C. elegans* oocytes [72]. Thus, it is possible that microtubules can provide Pickering agents in the mature Bb condensate.

Mechanistically, microtubules could directly serve as Pickering agents around the mature Bb, or indirectly provide an unknown Pickering agent by its supply to the Bb. Several observations argues for a direct mechanism. First, the cage-like organization of microtubules around the mature Bb suggests their physical role. Second, the mature stable and non-dynamic solid-like Bb condensate, exhibits low turnover with the cytoplasm, as shown by our work in zebrafish, as well as by that of others in *Xenopus*[46], and therefore supply of secondary agents is likely limited. Finally, the coarsening of the Bb over the course of 90 minutes upon microtubule depolymerization in our experiments is consistent with the timeframe of P granule coarsening upon loss of a direct Pickering agent in *C. elegans*[72]. These direct and indirect mechanisms are not mutually-exclusive and can contribute cooperatively in controlling the mature Bb condensate. However, it is likely that solid-like microtubule cables could at least partly directly serve as a Pickering agent to prevent the coarsening of the Bb (Fig. 7D, right). In the future, determining the precise mechanisms that could contribute to Bb overgrowth upon loss of microtubule, additionally to Ostwald ripening (as discussed above), will allow investigation of their control by possible further microtubule regulation.

All in all, the multiple regulatory steps by microtubules we uncovered ensure the formation of a single intact Bb condensate (Fig. 7D), which is essential for oocyte polarization and development. Our work raises several new concepts as discussed below.

Our work offers the new paradigm that phase-separation processes are under tight multi-step cellular control. Phase-separation processes have been often viewed as self-assembly reactions. However, their control is especially important where the extent and position of the condensate is critical, such as in the context of cellular polarization. The control over Bb condensation by microtubules serves this purpose in oocyte polarization. Data from mammalian epithelial polarity supports this notion. In polarized epithelia, the localization of the Cobl protein to the apical junction complex through microtubules is essential[73]. In vitro TIRF studies showed that Cobl condenses on microtubule cables that are pre-formed on glass slides[73], indicating that microtubule could control Cobl condensation towards localization to apical junctions[73]. Thus, the mechanisms of microtubule control over phase-separation that we uncovered directly in vivo, are likely relevant widely in biology.

The uncovered mechanisms shed new light on the roles of microtubules in molecular condensates. Studies in-vitro and in cell culture increasingly reveal the involvement of microtubules in molecular condensation[74,75], but those mostly show how condensates control microtubule nucleation or bundling[74,75], such as in the case of EB1[76], Tau[77-79] or LEM2[80] proteins. While reciprocal effects were postulated[75], we unequivocally uncover in vivo, how microtubule control various aspects of condensation in developmental physiological conditions, including the localization of the condensate by trafficking, its maintenance by serving as crowding agents, and its restriction by providing Pickering agent/s to prevent its coarsening.

Microtubules could control dynamic liquid-liquid phase-separation in additional ways. Our data shows that the dynein complex traffics condensing Buc granules on microtubules. It is also possible that the association of Buc complexes with dynein on microtubes creates high local concentration of Buc, above a threshold that promotes condensation. In the in-vitro Cobl studies mentioned above[74], lower total concentrations of Cobl were required for phase-separation on microtubules, and microtubules could replace PEG as a crowding agent in the solution[74]. Our data in vivo could not determine whether in addition to localizing Buc granules, dynein-mediated microtubule association also promotes Buc condensation per-se. However, the latter is consistent with the function of microtubules as crowding agents that we uncovered later in Bb condensation, suggesting that this is possible in vivo.

The multi-step control of Bb condensation by microtubules is highly relevant for understanding the underlying mechanisms of neurodegenerative disease, in which molecular condensation is thought to play an important role[81]. First, it was shown that the TDP-43 and FUS proteins can condense on microtubule cables in-vitro or in cells[82] and the Alzheimer's associated protein Tau is a microtubule binding protein[79]. Second, the dynamics of Bb condensation that we uncovered, whereby Buc undergoes early liquid-liquid phase-separation and later hardens by liquid-solid phase-separation that results in presumptive amyloid formation, is strikingly similar to Tau and α-Syn dynamics in in-vitro and cell culture models of Alzheimer's and Parkinson's diseases. Tau was shown to undergo liquid-liquid phase-separation that then promotes the crowding of amyloid promoting elements[77,79], and to coacervate with RNA[78]. α-Syn was shown in vitro to undergo early liquid-liquid phase-separation and later liquid-solid phase-separation that hardens into hydrogels and forms amyloid fibrils[65].

In cells, α-Syn condensed into small and dynamic liquid droplets within 24 hours from delivery, which then coalesced into a stationary main condensate within 48 hours[65], exemplifying the gradual prolonged process, as we show in vivo for the Bb. Moreover, the movement of early α-Syn granules was proposed to be dependent on microtubules, and the main coalesced α-Syn condensate formed in a nuclear indentation[65] that was strikingly similar to the nuclear cleft in oocytes ([12] and this study). Thus, both the dynamics and morphology of the α-Syn condensate present outstanding resemblance to those of the Bb. Notably, the Bb forms and functions in a regulated manner during development, and is a transient organelle that disassembles at the appropriate developmental stage, emphasizing its reversibility in physiological condition. This highlights the importance of deciphering Bb regulatory mechanisms as platform to uncover principles of molecular condensation that applies directly to neurodegenerative disease.

Our work provides the mechanisms of Bb formation in vertebrates, addressing a two-centuries old question since the discovery of the Bb in 1845[10]. In fish, frogs, and most vertebrates, the Bb stores RNA and proteins of maternal embryonic regulators, including the essential determinants of the dorsal and germ cell fates[1-3]. The Bb stores those during oocyte growth and then delivers them to the oocyte vegetal pole[1-3]. After delivery, essential RNP complexes, remain at the vegetal pole of the future embryo from which they orchestrate axis formation[1-3]. The mechanisms we uncover here decipher the source of embryonic polarity in vertebrates.

Our new insight into the Bb sheds new light on oocyte biology from insects to humans, where the Bb is conserved. In zebrafish, mice and humans, the Bb exhibit similar developmental dynamics at equivalent stages of oogenesis[10,12,13,15,16]. Further, the oocyte symmetry-breaking event that leads to Bb formation at the onset of meiosis, whereby Bb granules first localize around the oocyte centrosome, is conserved in insects, zebrafish and mice[12,15,83]. Those conserved features of the Bb strongly suggest that the mechanisms of Bb formation by molecular condensation and their control by microtubules that we uncovered, are conserved in mammals and are directly relevant to human female reproduction. Furthermore, molecular condensates were only previously identified in isolated fully-grown mammalian oocytes from fully-developed ovary[61]. Our findings uncover molecular condensation as an overlooked phenomena in the developing vertebrate ovary.

A better understanding of Bb regulation is needed for advancing our knowledge on female reproduction. Buc is the single known essential protein for the Bb in any species. Previous attempts to identify Buc-interacting regulators identified only two proteins, Rbpms2[84] and Tdrd6a[85]. However, loss of Rbpms2 was dispensable for Bb formation[84], and loss of Tdrd6a modified Buc aggregation, which affected Bb morphology, but did not prevent its formation[85]. Asz1 is a third protein that was known to localize to the Bb in fish and frogs[12,86,87] and to exhibit co-dynamics with the forming Bb in zebrafish[33], but we recently determined that despite other functions in germ cell and gonad development, Asz1 is also dispensable for Bb formation[88]. Our new lists of Bb Buc-interacting proteins that are present at the correct time and place in oocyte development, now provide promising stepping stones for identifying essential regulators of Bb formation. The principles and mechanisms of Bb condensation that we identified here, provide the correct framework for investigation. Thus, our work provides a leap forward in deciphering regulatory mechanisms of Bb formation and function, as well as oogenesis, and female reproduction.

Methods

Ethics statement

All animal experiments were supervised by the Hebrew University Authority for Biological Models, according to IACUC and accredited by AAALAC. All experiments were appropriately approved under ethics requests MD-18-15600-2.

Fish lines and gonad collections

Juvenile ovaries were collected from 5-7 week post-fertilization (wpf) juvenile fish. Fish had a standard length (SL) measured according to[89] and were consistently ~10-15mm. Ovary collection was done as in[8,12]. Briefly, to fix the ovaries for immunostaining, fish were cut along the ventral midline and the lateral body wall was removed. The head and tail were removed and the trunk pieces, with the exposed abdomen containing the ovaries, were fixed in 4% PFA at 4°C overnight with nutation. Trunks were then washed in PBS and ovaries were finely dissected in cold PBS. Ovaries were washed in PBS and then either stored in PBS at 4°C in the dark, or dehydrated and stored in 100% MeOH at -20°C in the dark.

Fish lines used in this research are: Tü *wt*, *Tg(buc:buc-gfp-buc 3'utr*) (Riemer et al., 2016)[90], *buc*^{p43} (Bontems et al., 2009)[91] and *Tg(bact:EMTB-3XGFP)* (Revenu et al., 2014)[92], *Tg(vasa:GFP)*[59].

Genotyping

Genotyping was performed at 4 wpf and over maximum of 2 days, after which fish were rested and raised in the system until the collection of their ovaries at 5-7 wpf. Fish were anaesthetized in 0.02% Tricaine in system water (Sigma Aldrich, #A5040), and a piece of their fin tail was clipped for DNA extraction. DNA was extracted using the standard *HotSHOT* DNA preparation method. *Tg(buc:Buc-GFP)* and *Tg(vasa:GFP)* fish were genotyped by genomic PCR, using PCRBIO HS Taq Mix Red (PCR Biosystems #PB10.13-02), and primers targeting the *gfp* sequence: forward: GACGTAAACGGCCACAAGTTCAG, reverse: GTTCACCTTGATGCCGTTCTTC. *buc*^{p43} mutant fish were genotyped by KASP genotyping (LGC, Teddington, UK). KASP-PCR was performed on an Applied Biosystems StepOnePlus machine and following the manufacturer instructions, and the SNP primer sequence:

ATCCACTCTGTTGCCCCCACAAAACTATTTGTCCTCAATTGGCAGTGCTTATTCCTACAGCTA[C/A]
TACCCACAAGTGACCCAAGAGCGCCAGAGTGTCTTAAGTCCATCCATAGATGAGCTCTCC.

Fluorescence immunohistochemistry (IHC) and HCR-FISH

Fluorescence immunohistochemistry (IHC) was performed as in[8,12]. Briefly, ovaries were washed 2 times for 5 minutes (2x5min) in PBT (0.3% Triton X-100 in 1xPBS; if stored in MeOH, ovaries were gradually rehydrated first), then washed 4x20min in PBT. Ovaries were blocked for 1.5-2hrs in blocking solution (10% FBS in PBT) at room temperature, and then incubated with primary antibodies in blocking solution at 4°C overnight. Ovaries were washed 4x20min in PBT and incubated with secondary antibodies in fresh blocking solution for 1.75hr, and were light protected from this step onward. Ovaries were washed 4x20min in PBT and then incubated in PBT containing DAPI (1:1000, Molecular Probes), with or without DiOC6 (1:5000, Molecular Probes) for 50min and washed 2x5min in PBT and 2x5min in PBS. All steps were carried out with nutation. Ovaries were transferred into Vectashield (with DAPI, Vector Labs). Ovaries were finally mounted between two #1.5 coverslips using a 120μm spacer (Molecular Probes).

Primary antibodies used were mouse anti-GFP (1:300; Molecular Probes), rabbit anti-GFP (1:400; Molecular Probes) and rabbit anti-Buc[63] (1:500; Yenzym Antibodies LLC), γTubulin (1:400, Sigma-Aldrich), mAb414 (1:1000, Abcam), dynein heavy chain DYNC1H1[62] (1:1000; Proteintek). Secondary antibodies used were Alexa Fluor 488 and 594 (1:500; Molecular Probes). Vital dyes used were: DiOC6 (1:5000, Molecular Probes)[8,12], Mitotracker (1:2000, Molecular Probes).

RNA-FISH for *dazl* mRNA was performed using the DNA-HCR-FISH technique (Molecular Instruments)[93], as in[8,12] and following the company protocol, except for the hybridization temperature that was optimized for 45ºC.

Confocal microscopy

Images were acquired on a Zeiss LSM 880 confocal microscope using a 40X lens. The acquisition setting was set between samples and experiments to: XY resolution=1104x1104 pixels, 12-bit, 2x sampling averaging, pixel dwell time=0.59sec, zoom=0.8X, pinhole adjusted to 1.1μm of Z thickness, increments between images in stacks were 0.53μm, laser power and gain were set in an antibody-dependent manner to 4-9% and 400-650, respectively, and below saturation condition. Unless otherwise noted, shown images are partial Sum Z-projection. Acquired images were not manipulated in a non-linear manner, and only contrast/brightness were adjusted. All figures were made using Adobe Photoshop CC 2014.

Confocal live and time-lapse imaging of cultured ovaries

Confocal live and time-lapse imaging of cultured ovaries was performed as in[8,94]. Briefly, ovaries were dissected from juvenile fish (5- 7wpf, SL~10-15mm) into fresh warm (28°C) HL-15 media (Hanks solution containing 60% L-15 (no phenol red), Sigma-Aldrich, and 1:100 Glutamax, Invitrogen, warmed to 28°C). Ovaries were then embedded in 0.5% low-melt agarose in HL-15 on a glass-bottom dish, and covered with warm HL-15. After the agarose polymerized, ovaries were incubated in HL-15 at 28°C. Time-lapse images of live ovaries were acquired using either a Zeiss LSM 880 or Nikon Ti2E spinning disc confocal microscopes, both equipped with an environmental chamber set to 28°C, and using a 40X and 60X objectives, respectively.

Images were acquired every 6 seconds for single Z section, or 18-20 seconds for Z stacks, over 5-10min.

Super-resolution microscopy

For super-resolution microscopy, we used a dSTORM system and protocol as described in[95], which allows for imaging at approximately 20 nm resolution. All dSTORM imaging was performed on TIRF mode. Whole *Tg(βact:EMTB-3XGFP)* juvenile ovaries were immunostained, using primary mouse anti-GFP (1:500; Molecular Probes) and rabbit anti-Buc (1:500; polyclonal antibodies against N-term, Buc peptide Yenzym Antibodies LLC) antibodies. Secondary antibodies used were anti-rabbit H+L Alexa Fluor 568 and anti-mouse H+L Alexa Fluor 488 (1:500; Life Technologies). After IHC, ovaries were then mounted on poly-D-lysine coated coverslips (no. 1.5H, Marienfeld-superior, Lauda-Königshofen, Germany). dSTORM imaging was performed in a freshly prepared imaging buffer containing 50 mM Tris (pH 8.0), 10 mM NaCl and 10% (w/v) glucose with an oxygen-scavenging GLOX solution (0.5 mg/ml glucose oxidase (Sigma-Aldrich), 40 µg/ml catalase (Sigma-Aldrich), 10 mM cysteamine MEA (Sigma-Aldrich) and 1% β- mercaptoethanol. A Nikon Ti-E inverted microscope was used. The N-STORM Nikon system was built on TIRF illumination using a 1.49 NA 100X oil immersion objective and an ANDOR DU-897 camera. 488 , 568 nm laser lines were used for activation with cycle repeat of ∼4000 cycles for each channel. Nikon NIS Element software was used for acquisition and analysis. A gaussian visualization is shown in images in Fig. 3H, in which signal intensity correlates with localization precision. 'Cross-visualization' in Fig. S4D shows all resolved signals where each single-molecule signal displays as a cross in the N-STORM software.

Drug Treatments

Ovaries were dissected from wt, *Tg(buc:buc-gfp-buc 3'utr)*, or *Tg(bact:EMTB-3XGFP)* juvenile fish (5-7 wpf, SL ~10-15mm) into fresh warm (28°C) HL-15 media as described in (Elkouby & Mullins, 2017b). Then HL-15 was replaced with HL-15 containing the drug of interest. For microtubule depolymerization and dynein inhibition, we used either 20µM nocodazole (Abcam #ab120630), 50µM colchicine (Sigma Aldrich #C9754), 40µM taxol (Abcam #ab120143), 25µM ciliobrevin (Sigma Aldrich #250401), or an equivalent volume of DMSO as vehicle control. Each drug treatment experiment contained a DMSO control group and for microtubule manipulating drugs also a *Tg(bact:EMTB-3XGFP)* sample as readout of the effects on microtubule. Ovaries were incubated for 90min at 28°C in the dark. Ovaries were then mounted for live imaging in media containing their respective drug concentration or DMSO control. Under these conditions, ovaries are normally viable for at least 8hrs[8], and their viability was verified by MitoTracker Mitochondria-Selective Probes (500nM, Molecular Probes #M7512). At the end of treatments, ovaries were either continued to be imaged live, or fixed for analyses. For 1,6-hexanediol, live ovaries were similarly dissected. Ovaries were incubated in either 5% or 10% 1,6-hexanediol (Sigma, #240117) or equivalent volumes of MeOH as vehicle control, and either imaged live for 90 minutes while recording full z-stacks every 10 minutes, or treated for 90 minutes and then fixed for *dazl* HCR-FISH.

Thioflavin (ThT)

Ovaries were dissected from wt, *Tg(buc:buc-gfp-buc 3'utr)*, or *buc*$^{-/-}$ juvenile fish (5-7 wpf, SL ~10-15mm) into fresh warm (28°C) HL-15 media as described above and in (Elkouby & Mullins, 2017b). Ovaries were incubated with 20µM ThT (Sigma Aldrich #T3516) for 30 minutes and then rinsed x2 in fresh warm HL-15 media before being mounted for live imaging or fixed for staining.

Stage Specific Oocyte Isolation

Ovaries were collected from adult females at 6-8 months post-fertilization. Stage specific oocyte isolation from ovaries was performed as described in[8,50]. Briefly, oocytes are first isolated from ovaries by short enzymatic digestion (3 mg/ml Collagenase I, Sigma-Aldrich, #C0130; 3 mg/ml Collagenase II, Sigma-Aldrich, #C6885; 1.6 mg/ml Hyaluronidase, in HL-15, Sigma-Aldrich, #H4272), at 28°C and in HL-15. Isolated oocytes are separated by size using cell strainers in various pore sizes (BD Falcon), and washed in HL-15. Oocytes are then immediately lysed for biochemical experiments, or cultured in HL-15 at 28°C for live experiments.

Oocyte lysis and separation of pellet and supernatant fractions

Stage specific oocytes were isolated as described above and were homogenized with a micro-pestle on ice in lysis buffer [10mM Tris (pH 7.5), 150mM NaCl, 0.5mM EDTA, 0.5% NP-40, 1X complete protease inhibitor cocktail (Roche, Mannheim)] according to (Riemer et al., 2015). After lysis, samples were spun down 10min at 12,000 x g at 4°C and the subsequent supernatant and pellet fractions were isolated separately for western blot and/or mass-spectrometry analyses. In figure 2B, L-Arginine (Sigma Aldrich #5131) was added directly to the lysis buffer, prior to starting the western blot protocol.

Immunoprecipitation

Each immunoprecipitation sample was performed on oocytes isolated from 4 whole ovaries, which were dissected from 2 fish, as described above. Samples were lysed in 650 mL lysis/IP buffer [10mM Tris (pH 7.5), 150mM NaCl, 0.5mM EDTA, 0.5% NP-40, 1X complete protease inhibitor cocktail (Roche, Mannheim)] according to (Riemer et al., 2015) and homogenized with a micro-pestle followed by sonication for 3 x 30sec at low power. 25µl of GFP-Trap beads (GFP-Trap Dynabeads, Chromotek #gtd-20) per lysate were used for GFP pulldown from experiment *Tg(buc:Buc-GFP)*, as well as *wt* no transgenic GFP control, and *Tg(vasa:GFP)* free GFP control samples, and 25µl of control no-GFP nanobody beads (Chromotek), were used for IP control on *Tg(buc:Buc-GFP)* samples. Samples were then incubated for 1hr at 4°C, followed by 3 washes with wash buffer before western blot, mass-spectrometry, or dot blot analyses. Each sample (Buc-GFP-IP, and the three controls: no GFP-IP, beads only-IP, and free-GFP-IP), were performed in biological triplicates and the entire experiment was performed at least three times.

Mass-Spectrometry Analysis

All MS samples were performed and analyzed at the Smoler Proteomics Centre at the Technion (Haifa, Israel). The samples were precipitated in 80% acetone, and washed 4 times with cold 80% acetone. The protein pellets were dissolved in 8.5M Urea and 400mM ammonium bicarbonate and 10mM DTT. The samples were reduced (60ºC for 30min), modified with 35.2mM iodoacetamide in 100mM ammonium bicarbonate (RT for 30min in the dark) and digested in 1.5M Urea, 66mM ammonium bicarbonate with modified trypsin (Promega), overnight at 37^{o}C in a 1:50 (M/M) enzyme-to-substrate ratio. An additional second trypsinization was done for 4hrs. The resulting tryptic peptides were desalted using C18 tips (Home-made stage tips), dried and re-suspended in 0.1% Formic acid. They were analyzed by LC-MS/MS using Q Exactive HFX mass spectrometer (Thermo) fitted with a capillary HPLC (easy nLC 1000, Thermo). The peptides were loaded onto a homemade capillary column (20 cm, 75micron ID) packed with Reprosil C18-Aqua (Dr. Maisch GmbH, Germany) in solvent A (0.1% formic acid in water). The peptides mixture was resolved with a (5 to 28%) linear gradient of solvent B (95% acetonitrile with 0.1% formic acid) for 120min followed by gradient of 15min gradient of 28 to 95% and 15min at 95% acetonitrile with 0.1% formic acid in water at flow rates of 0.15μl/min. Mass spectrometry was performed in a positive mode using repetitively full MS scan followed by high collision induces dissociation (HCD, at 25 normalized collision energy) of the 10 most dominant ions (>1 charges) selected from the first MS scan. The mass spectrometry data was analyzed using the MaxQuant software 1.5.2.8. (//www.maxquant.org) using the Andromeda search engine, searching against the *Danio rerio* proteome from the Uniprot database with mass tolerance of 4.5ppm for the precursor masses and 4.5ppm for the fragment ions. Peptide- and protein-level false discovery rates (FDRs) were filtered to 1% using the target-decoy strategy. Protein table was filtered to eliminate the identifications from the reverse database, common contaminants and single peptide identifications. The data was quantified by label free analysis using the same software, based on extracted ion currents (XICs) of peptides enabling quantitation from each LC/MS run for each peptide identified in any of experiments. Statistical analysis of the identification and quantization results was done using Perseus 1.6.7.0 software.

Bioinformatical Analysis

Primary Statistical analysis was performed using Perseus 1.6.7.0 software. Differential expression of proteins has been calculated manually using Excel. For Sup/Pel and Buc-IP experiment, LFQ intensities of identified proteins for all samples were log normalized. To identify differentially enriched proteins, pairwise comparison was performed between experiment and control samples, using the formula *log2(Fold Change) = log2(protein intensity of sample1 / protein intensity of sample2)*, *p*-values were calculated by students t-test between samples. For Sup/Pel experiment pairwise comparison of fold change and *p*-value were calculated between *wt* sup Vs. *wt* pellet and *buc*$^{-/-}$ sup Vs. *buc*$^{-/-}$ pellet. For Buc-IP experiments, pairwise comparison of fold change and *p*-value were calculated between the Buc-GFP Vs. all other control samples. The cutoff for fold change has been set as 2 and for *p*-value<0.05. Enriched proteins for both sup/pel and BUC-IP experiments were visualized by Volcano Plots using the R-based software VolcanoseR[96]. Heatmaps and hierarchical clustering of enriched proteins ere generated using R and the R-based software ClustVis[97].

Gene Ontology Analysis

Gene ontology analysis of enriched Bb resident and identified Buc binding proteins was performed using the software ShinyGo[98] gene ontology database. The cut off for the FDR has been set as FDR<0.05.

Computational analyses of IDR and PLD

Primary sequences of enriched Bb resident and Buc binding proteins were taken from UniPort[99] as FASTA sequence format and analyzed using three different algorithms, PONDR[100], FoldIndex[101] and ESpritz[102], independently to predict protein ordered and disordered regions. PLAAC[103] software was used to identify sequences of prion like domains in those proteins.

Western Blot analysis

Samples were heated to 95°C with 2X sample buffer (4X stock contains: 40% glycerol, 0.2M Tris pH 6.8, 20% ß-mercaptanol, 4% SDS and 0.005% Bromophenol Blue) for 5min prior to loading on a 4%-20% Mini-PROTEAN TGX gels (BioRad, #456-1094) and blotted using Trans-Blot Turbo Transfer Pack 0.2µm nitrocellulose (BioRad, #1704159) on the TransBlot Turbo BioRad system at 2.5A, 23V for 10min. Membranes were blocked for 2hrs at RT in 5% milk powder and then incubated overnight (o/n) at 4°C with primary rabbit anti-GFP antibody

(1:1,000; Molecular Probes). Membranes were washed 3x for 10min in 1X TBST. Membranes were then incubated with the secondary antibody, peroxidase-conjugated AffiniPure Goat Anti-Rabbit IgG (H+L) (Jackson ImmunoResearch, #111-035-003), for 1hr at RT. Membranes were finally washed 5x for 5min in 1XTBST before being developed with the ECL Clarity Kit (BioRad) and imaged on ChemiDoc Imaging Systems (BioRad). Images were analyzed on Image Lab 4.1 (BioRad).

Dot Blot analysis

After Immunoprecipitation, samples were heated to 95°C with 2X sample buffer for 5 mins before loading the samples directly to a 0.2µm nitrocellulose (BioRad, #1704159) membrane. Membranes were cut as thin strips and grid lines have been drawn with pencil on the membrane. 10µl of each sample were directly loaded on each grid on the membrane and the membrane was air dried. Membranes were then blocked for 1 hour at RT in 5% milk powder and then incubated overnight (o/n) at 4°C with primary antibodies. Antibodies used were rabbit anti-GFP antibody (1:1,000; Molecular Probes), rabbit anti-DYNC1H1 antibody (1:1000; Proteintek), and mouse anti-b-Actin antibody (Jackson ImmunoResearch, #111-035-003). Membranes were washed 3x for 10min in 1X TBST and incubated with the secondary antibody, peroxidase-conjugated AffiniPure Goat Anti-Rabbit IgG (H+L) (Jackson ImmunoResearch, #111-035-003), or peroxidase-conjugated AffiniPure Goat Anti-Mouse IgG (H+L) (Jackson ImmunoResearch, #115-035-003) for 2hr at RT. Membrane strips were finally washed 6x for 3mins in 1X TBST before being developed with the ECL Clarity Kit (BioRad) and imaged on ChemiDoc Imaging system (BioRad). Images were analyzed on Image Lab 4.1 (BioRad).

Fluorescence Recovery After Photobleaching (FRAP)

FRAP was performed on a Zeiss LSM 880 confocal microscope in ovaries carrying Buc-GFP transgene [*Tg(buc:buc-gfp-buc 3'utr*]. In preperation experiments, we established that bleaching 1/3 of the aggregate resulted in a significant reduction in Buc-GFP signal without completely ablating all the protein in the nuclear cleft. Furthermore, we observed a plateau of recovery dynamics after 680sec, and therefore to reduce any photobleaching affects, all experiments had a total duration of 680sec. Based on these calibration experiments, in all experiments we systemically bleached an area of approximately 1/3 of the aggregate size to around 20% of the original Buc-GFP intensity and then followed recovery for 680 seconds (11.33min), recording every 2.5 second. Regions (pre– and post-bleach) were tracked using ROI manager on Fiji. 10 pre-bleach frames were recorded and after background subtraction, the average intensity was used as pre-bleach intensity. Post-bleach frames were background subtracted and to make replicates comparable, post-bleach frame #1 of each measurement was set to 0 and corresponding pre-bleach intensity was corrected for this. Subsequently, recovery curves were plotted and the immobile/mobile fractions were calculated (see below) in order to determine Buc protein dynamics and turnover within individual oocytes. Mobile and Immobile fractions were calculated according to European Advanced Light Microscopy Network (EAMNET):

$$\text{Mobile fraction } F_m = (I_E - I_0) / (I_{we} - I_0)$$

$$\text{Immobile fraction } F_i = 1 - Fm$$

I_E is the end value of the recovered fluorescence intensity, I_0 is the first postbleach fluorescence intensity, and I_I is the initial (prebleach) fluorescence intensity.

Measurements of Buc intensity plots in the cleft

To analyze Buc condensates in the forming Bb, we analyzed the intensity and distribution of Buc-GFP signals in the cleft. The cleft was identified by antibody labeling detecting two landmarks: *1)* mAb414, detecting FG repeats in nuclear pore complexes and delineating the nuclear envelop (NE), and *2)* γTub, detecting the centrosome at the vicinity of the cleft, where Buc localizes. We identified the optical z-section in which the cleft was most pronounced based on the NE mAb414 signal, or the one that included the centrosome, both indicating the approximate center of the cleft and the main Buc condensate. We generated max z-projection images of three optical sections, including the one of the cleft center as identified above, as well as one below and one above it. We measured Buc intensities and distribution in the cleft, using the Fiji software. We drew a 9 µm line between the nuclear protrusions that encapsulated the cleft, and across the Buc condensate. Based on analyses on oocytes at these stages in preparation experiments, we determined that a line of 9 µm in length consistently spans the entire cleft opening and covers the main Buc condensate. The measuring line was divided into 37 bins every 0.24 µm and the intensity of Buc-GFP was measured at each bin. Buc-GFP signals at each bin were first background subtracted and then normalized. For measuring Buc-GFP background, we measured its intensity in a square (20 µm^2) drawn in the oocyte nucleus, where Buc should not localize. To control for immune-labeling variation, background subtracted Buc-GFP signals were normalized to the mean intensity/area of co-labeled mab414 or γTub signals. Normalized Buc-GFP intensity were plotted along the measuring line for each oocyte. Pooled data was plotted as mean ± SD for each experiment and between experiments.

Three-dimensional analysis of Buc in IMARIS

Confocal raw data images of entire z-stacks of oocytes were extracted from whole ovary images and imported to IMARIS. Nuclei, centrosomes and Buc condensates were segmented in 3D using blend volume rendering mode, and signal brightness and object transparency were slightly and linearly adjusted in all channels to optimize visualization. Animation frames were made using the key frame animation tool and surfaces of centrosomes and Buc-GFP granules were generated. The threshold absolute intensity of Buc-GFP was set as 0.22 of Buc-GFP maximum intensity and the threshold of voxels was set as 0.003 of the maximum voxel number, for all oocytes across samples and experiments. To analyze Buc-GFP granules, their automatically generated number and surface area were extracted from IMARIS. To analyze the distance between Buc granules and the centrosome, the distance between the center of the mass of the centrosome and the center of mass of each Buc granule was measured in IMARIS. Measured parameters were exported to Excel and GraphPad Prism for statistical analyses and plotting.

Coarsening experiments and IMARIS analyses

Ovaries were dissected from *Tg(buc:buc-gfp-buc3'utr*), and *Tg(bact:EMTB-3XGFP)* adult fish into fresh warm HL-15 media as described in[8]. Ovaries were digested and oocytes at sizes of 50-100 μm were isolated as described above in the stage specific oocyte isolation section. After isolation, oocytes were embedded in low melt agarose with 20 μM nocodazole or DMSO in glass bottom dish and the dish was filled with HL-15 medium containing 20 μM nocodazole or DMSO, respectively. Oocytes from *EMTB-3XGFP* and *Buc-GFP* ovaries were incubated at 28ºC in the dark and treated side by side, and the *EMTB-3XGFP* oocytes were imaged to monitor microtubules depolymerization. The time point of microtubule depolymerization (after ~1 hour), as detected in the *EMTB-3XGFP* sample, was set as T_0 for Buc-GFP oocytes, which were then imaged for 1.5 hours, while recording z-stacks every 1 min. Live imaging was performed on a spinning disc confocal microscope. Live time-lapse images were exported to IMARIS for further analysis.

In the IMARIS software, each oocytes and their respective Bbs were segmented throughout the Z axis, and the *1)* volume, *2)* surface area and *3)* the intensity of Buc-GFP were recorded throughout the course of the 1.5 hours of imaging. Next, the absolute volume (V_{Bb}), Surface area (SA_{Bb}) and the Intensity (I_{Bb}) of Bbs, as well as the volume (V_O), Surface area (SA_O) and the Intensity (I_O) of their corresponding oocytes were recorded over time. The absolute volume, surface area and intensity were normalized to the oocyte volume, surface area and the intensity respectively. The density of the Bb was calculated using the normalized intensity of Bbs over their normalized volume, as follows:

$$\text{Normalized Volume of Bb } (NV_{Bb}) = (V_{Bb}) / (V_O)$$

$$\text{Normalized Surface area of Bb } (NSA_{Bb}) = (SA_{Bb}) / (SA_O)$$

$$\text{Normalized Intensity of Bb } (NI_{Bb}) = (I_{Bb}) / (I_O)$$

$$\text{Normalized Density of Bb } (ND_{Bb}) = (NI_{Bb}) / (NV_{Bb})$$

Next, the Fold change of the normalized volume, surface area and the density were calculated by dividing these normalized parameters at each time point (T_i) to these normalized parameters at the starting time point (T_0), as follows:

$$\text{Fold Change of Bb volume } (FCV_{Bb}) = (NV_{Bb}) \text{ at } T_i / (NV_{Bb}) \text{ at } T_0$$

$$\text{Fold Change of Bb surface area } (FCSA_{Bb}) = (NSA_{Bb}) \text{ at } T_i \,/\, (NSA_{Bb}) \text{ at } T_0$$

$$\text{Fold Change of Bb density } (FCND_{Bb}) = (ND_{Bb}) \text{ at } T_i \,/\, (ND_{Bb}) \text{ at } T_0$$

Finally, the fold change values of these parameters were plotted as the mean ±SD, over time.

Statistical Analysis

All statistical analysis and data plotting were performed using the GraphPad Prism 7 software and Microsoft Excel. Data sets were tested with two-tailed unpaired t-test. *p*-values were: *<0.01,****<0.05).

References

1. Jamieson-Lucy, A., and Mullins, M.C. (2019). Chapter One - The vertebrate Balbiani body, germ plasm, and oocyte polarity. In Current Topics in Developmental Biology, R. Lehmann, ed. (Academic Press), pp. 1-34. https://doi.org/10.1016/bs.ctdb.2019.04.003.
2. Escobar-Aguirre, M., Elkouby, Y.M., and Mullins, M.C. (2017). Localization in Oogenesis of Maternal Regulators of Embryonic Development. In Vertebrate Development: Maternal to Zygotic Control, F. Pelegri, M. Danilchik, and A. Sutherland, eds. (Springer International Publishing), pp. 173-207. 10.1007/978-3-319-46095-6_5.
3. Langdon, Y.G., and Mullins, M.C. (2011). Maternal and zygotic control of zebrafish dorsoventral axial patterning. Annu Rev Genet *45*, 357-377. 10.1146/annurev-genet-110410-132517.
4. Krishnakumar, P., Riemer, S., Perera, R., Lingner, T., Goloborodko, A., Khalifa, H., Bontems, F., Kaufholz, F., El-Brolosy, M.A., and Dosch, R. (2018). Functional

equivalence of germ plasm organizers. PLOS Genetics *14*, e1007696. 10.1371/journal.pgen.1007696.

5. Boke, E., Ruer, M., Wühr, M., Coughlin, M., Lemaitre, R., Gygi, S.P., Alberti, S., Drechsel, D., Hyman, A.A., and Mitchison, T.J. (2016). Amyloid-like Self-Assembly of a Cellular Compartment. Cell *166*, 637-650. 10.1016/j.cell.2016.06.051.

6. Dosch, R., Wagner, D.S., Mintzer, K.A., Runke, G., Wiemelt, A.P., and Mullins, M.C. (2004). Maternal control of vertebrate development before the midblastula transition: mutants from the zebrafish I. Dev Cell *6*, 771-780. 10.1016/j.devcel.2004.05.002.

7. Marlow, F.L., and Mullins, M.C. (2008). Bucky ball functions in Balbiani body assembly and animal-vegetal polarity in the oocyte and follicle cell layer in zebrafish. Dev Biol *321*, 40-50. 10.1016/j.ydbio.2008.05.557.

8. Elkouby, Y.M., and Mullins, M.C. (2017). Methods for the analysis of early oogenesis in Zebrafish. Dev Biol *430*, 310-324. 10.1016/j.ydbio.2016.12.014.

9. Jamieson-Lucy, A., and Mullins, M.C. (2019). The vertebrate Balbiani body, germ plasm, and oocyte polarity. Curr Top Dev Biol *135*, 1-34. 10.1016/bs.ctdb.2019.04.003.

10. Kloc, M., Bilinski, S., and Etkin, L.D. (2004). The Balbiani Body and Germ Cell Determinants: 150 Years Later. In Current Topics in Developmental Biology, G.P. Schatten, ed. (Academic Press), pp. 1-36. https://doi.org/10.1016/S0070-2153(04)59001-4.

11. Cox, R.T., and Spradling, A.C. (2003). A Balbiani body and the fusome mediate mitochondrial inheritance during Drosophila oogenesis. Development *130*, 1579-1590. 10.1242/dev.00365.

12. Elkouby, Y.M., Jamieson-Lucy, A., and Mullins, M.C. (2016). Oocyte Polarization Is Coupled to the Chromosomal Bouquet, a Conserved Polarized Nuclear Configuration in Meiosis. PLOS Biology *14*, e1002335. 10.1371/journal.pbio.1002335.

13. Hertig, A.T. (1968). The primary human oocyte: Some observations on the fine structure of Balbiani's vitelline body and the origin of the annulate lamellae. American Journal of Anatomy *122*, 107-137. https://doi.org/10.1002/aja.1001220107.

14. Pepling, M.E., Wilhelm, J.E., O'Hara, A.L., Gephardt, G.W., and Spradling, A.C. (2007). Mouse oocytes within germ cell cysts and primordial follicles contain a Balbiani body. Proceedings of the National Academy of Sciences *104*, 187-192. doi:10.1073/pnas.0609923104.

15. Lei, L., and Spradling, A.C. (2016). Mouse oocytes differentiate through organelle enrichment from sister cyst germ cells. Science *352*, 95-99. doi:10.1126/science.aad2156.

16. Amin, R., Bukulmez, O., and Woodruff, J.B. (2023). Visualization of Balbiani Body disassembly during human primordial follicle activation. microPublication Biology.

17. Elkouby, Y.M., and Mullins, M.C. (2017). Coordination of cellular differentiation, polarity, mitosis and meiosis – New findings from early vertebrate oogenesis. Developmental Biology *430*, 275-287. https://doi.org/10.1016/j.ydbio.2017.06.029.

18. Choi, J.M., Holehouse, A.S., and Pappu, R.V. (2020). Physical Principles Underlying the Complex Biology of Intracellular Phase Transitions. Annu Rev Biophys *49*, 107-133. 10.1146/annurev-biophys-121219-081629.

19. Dodson, A.E., and Kennedy, S. (2020). Phase Separation in Germ Cells and Development. Dev Cell *55*, 4-17. 10.1016/j.devcel.2020.09.004.

20. Mitrea, D.M., and Kriwacki, R.W. (2016). Phase separation in biology; functional organization of a higher order. Cell Commun Signal *14*, 1. 10.1186/s12964-015-0125-7.

21. Hyman, A.A., Weber, C.A., and Jülicher, F. (2014). Liquid-liquid phase separation in biology. Annu Rev Cell Dev Biol *30*, 39-58. 10.1146/annurev-cellbio-100913-013325.

22. Shin, Y., and Brangwynne, C.P. (2017). Liquid phase condensation in cell physiology and disease. Science *357*. 10.1126/science.aaf4382.

23. Boeynaems, S., Alberti, S., Fawzi, N.L., Mittag, T., Polymenidou, M., Rousseau, F., Schymkowitz, J., Shorter, J., Wolozin, B., Van Den Bosch, L., et al. (2018). Protein Phase Separation: A New Phase in Cell Biology. Trends Cell Biol *28*, 420-435. 10.1016/j.tcb.2018.02.004.

24. Rhine, K., Vidaurre, V., and Myong, S. (2020). RNA Droplets. Annual Review of Biophysics *49*, 247-265. 10.1146/annurev-biophys-052118-115508.

25. Roden, C., and Gladfelter, A.S. (2021). RNA contributions to the form and function of biomolecular condensates. Nat Rev Mol Cell Biol *22*, 183-195. 10.1038/s41580-020-0264-6.

26. So, C., Cheng, S., and Schuh, M. (2021). Phase Separation during Germline Development. Trends Cell Biol *31*, 254-268. 10.1016/j.tcb.2020.12.004.

27. Dignon, G.L., Best, R.B., and Mittal, J. (2020). Biomolecular Phase Separation: From Molecular Driving Forces to Macroscopic Properties. Annu Rev Phys Chem *71*, 53-75. 10.1146/annurev-physchem-071819-113553.

28. Hanazawa, M., Yonetani, M., and Sugimoto, A. (2011). PGL proteins self associate and bind RNPs to mediate germ granule assembly in C. elegans. Journal of Cell Biology *192*, 929-937. 10.1083/jcb.201010106.

29. Brangwynne, C.P., Eckmann, C.R., Courson, D.S., Rybarska, A., Hoege, C., Gharakhani, J., Jülicher, F., and Hyman, A.A. (2009). Germline P Granules Are Liquid Droplets That Localize by Controlled Dissolution/Condensation. Science *324*, 1729-1732. doi:10.1126/science.1172046.

30. Eichler, C.E., Li, H., Grunberg, M.E., and Gavis, E.R. (2023). Localization of oskar mRNA by agglomeration in ribonucleoprotein granules. PLOS Genetics *19*, e1010877. 10.1371/journal.pgen.1010877.

31. Valentino, M., Ortega, B.M., Ulrich, B., Doyle, D.A., Farnum, E.D., Joiner, D.A., Gavis, E.R., and Niepielko, M.G. (2022). Computational modeling offers new insight into&#xa0;Drosophila germ granule development. Biophysical Journal *121*, 1465-1482. 10.1016/j.bpj.2022.03.014.

32. Bose, M., Lampe, M., Mahamid, J., and Ephrussi, A. (2022). Liquid-to-solid phase transition of oskar ribonucleoprotein granules is essential for their function in Drosophila embryonic development. Cell *185*, 1308-1324.e1323. 10.1016/j.cell.2022.02.022.

33. Trcek, T., Douglas, T.E., Grosch, M., Yin, Y., Eagle, W.V.I., Gavis, E.R., Shroff, H., Rothenberg, E., and Lehmann, R. (2020). Sequence-Independent Self-Assembly of Germ Granule mRNAs into Homotypic Clusters. Molecular Cell *78*, 941-950.e912. 10.1016/j.molcel.2020.05.008.

34. Guo, L., and Shorter, J. (2015). It's Raining Liquids: RNA Tunes Viscoelasticity and Dynamics of Membraneless Organelles. Mol Cell *60*, 189-192. 10.1016/j.molcel.2015.10.006.

35. Villegas, J.A., Heidenreich, M., and Levy, E.D. (2022). Molecular and environmental determinants of biomolecular condensate formation. Nat Chem Biol *18*, 1319-1329. 10.1038/s41589-022-01175-4.

36. Tauber, D., Tauber, G., and Parker, R. (2020). Mechanisms and Regulation of RNA Condensation in RNP Granule Formation. Trends Biochem Sci *45*, 764-778. 10.1016/j.tibs.2020.05.002.

37. Li, J., Zhang, M., Ma, W., Yang, B., Lu, H., Zhou, F., and Zhang, L. (2022). Post-translational modifications in liquid-liquid phase separation: a comprehensive review. Mol Biomed *3*, 13. 10.1186/s43556-022-00075-2.

38. Putnam, A., and Seydoux, G. (2023). Chapter 13 - Intrinsically disordered regions: a platform for regulated assembly of biomolecular condensates. In Droplets of Life, V.N. Uversky, ed. (Academic Press), pp. 397-430. https://doi.org/10.1016/B978-0-12-823967-4.00016-6.

39. Wang, J.T., Smith, J., Chen, B.-C., Schmidt, H., Rasoloson, D., Paix, A., Lambrus, B.G., Calidas, D., Betzig, E., and Seydoux, G. (2014). Regulation of RNA granule dynamics by phosphorylation of serine-rich, intrinsically disordered proteins in C. elegans. eLife *3*, e04591. 10.7554/eLife.04591.

40. Murray, D.T., Kato, M., Lin, Y., Thurber, K.R., Hung, I., McKnight, S.L., and Tycko, R. (2017). Structure of FUS Protein Fibrils and Its Relevance to Self-Assembly and Phase Separation of Low-Complexity Domains. Cell *171*, 615-627.e616. 10.1016/j.cell.2017.08.048.

41. Jacobs, W.M. (2021). Self-Assembly of Biomolecular Condensates with Shared Components. Physical Review Letters *126*, 258101. 10.1103/PhysRevLett.126.258101.

42. Kato, M., Han, Tina W., Xie, S., Shi, K., Du, X., Wu, Leeju C., Mirzaei, H., Goldsmith, Elizabeth J., Longgood, J., Pei, J., et al. (2012). Cell-free Formation of RNA Granules: Low Complexity Sequence Domains Form Dynamic Fibers within Hydrogels. Cell *149*, 753-767. 10.1016/j.cell.2012.04.017.

43. Han, Tina W., Kato, M., Xie, S., Wu, Leeju C., Mirzaei, H., Pei, J., Chen, M., Xie, Y., Allen, J., Xiao, G., and McKnight, Steven L. (2012). Cell-free Formation of RNA Granules: Bound RNAs Identify Features and Components of Cellular Assemblies. Cell *149*, 768-779. 10.1016/j.cell.2012.04.016.

44. Jamieson-Lucy, A.H., Kobayashi, M., James Aykit, Y., Elkouby, Y.M., Escobar-Aguirre, M., Vejnar, C.E., Giraldez, A.J., and Mullins, M.C. (2022). A proteomics approach identifies novel resident zebrafish Balbiani body proteins Cirbpa and Cirbpb. Developmental Biology *484*, 1-11. https://doi.org/10.1016/j.ydbio.2022.01.006.

45. Bose, M., Lampe, M., Mahamid, J., and Ephrussi, A. (2022). Liquid-to-solid phase transition of oskar ribonucleoprotein granules is essential for their function in Drosophila embryonic development. Cell *185*, 1308-1324.e1323. https://doi.org/10.1016/j.cell.2022.02.022.

46. Chang, P., Torres, J., Lewis, R.A., Mowry, K.L., Houliston, E., and King, M.L. (2004). Localization of RNAs to the Mitochondrial Cloud in Xenopus Oocytes through Entrapment and Association with Endoplasmic Reticulum. Molecular Biology of the Cell *15*, 4669-4681. 10.1091/mbc.e04-03-0265.

47. Boke, E., and Mitchison, T.J. (2017). The balbiani body and the concept of physiological amyloids. Cell Cycle *16*, 153-154. 10.1080/15384101.2016.1241605.

48. Woodruff, J.B., Hyman, A.A., and Boke, E. (2018). Organization and Function of Non-dynamic Biomolecular Condensates. Trends in Biochemical Sciences *43*, 81-94. 10.1016/j.tibs.2017.11.005.

49. Wang, Z., Lou, J., and Zhang, H. (2022). Essence determines phenomenon: Assaying the material properties of biological condensates. Journal of Biological Chemistry *298*. 10.1016/j.jbc.2022.101782.

50. Bogoch, Y., Jamieson-Lucy, A., Vejnar, C.E., Levy, K., Giraldez, A.J., Mullins, M.C., and Elkouby, Y.M. (2022). Stage Specific Transcriptomic Analysis and Database for Zebrafish Oogenesis. Front Cell Dev Biol *10*, 826892. 10.3389/fcell.2022.826892.

51. Tsumoto, K., Umetsu, M., Kumagai, I., Ejima, D., Philo, J.S., and Arakawa, T. (2004). Role of Arginine in Protein Refolding, Solubilization, and Purification. Biotechnology Progress *20*, 1301-1308. https://doi.org/10.1021/bp0498793.

52. Hennig, S., Kong, G., Mannen, T., Sadowska, A., Kobelke, S., Blythe, A., Knott, G.J., Iyer, K.S., Ho, D., Newcombe, E.A., et al. (2015). Prion-like domains in RNA binding proteins are essential for building subnuclear paraspeckles. Journal of Cell Biology *210*, 529-539. 10.1083/jcb.201504117.

53. Krammer, C., Schätzl, H.M., and Vorberg, I. (2009). Prion-like propagation of cytosolic protein aggregates. Prion *3*, 206-212. 10.4161/pri.3.4.10013.

54. Blumenthal, D., Goldstien, L., Edidin, M., and Gheber, L.A. (2015). Universal Approach to FRAP Analysis of Arbitrary Bleaching Patterns. Sci Rep *5*, 11655. 10.1038/srep11655.

55. Giakoumakis, N.N., Rapsomaniki, M.A., and Lygerou, Z. (2017). Analysis of Protein Kinetics Using Fluorescence Recovery After Photobleaching (FRAP). Methods Mol Biol *1563*, 243-267. 10.1007/978-1-4939-6810-7_16.

56. Kang, M., Andreani, M., and Kenworthy, A.K. (2015). Validation of Normalizations, Scaling, and Photofading Corrections for FRAP Data Analysis. PLOS ONE *10*, e0127966. 10.1371/journal.pone.0127966.

57. Mytlis, A., Kumar, V., Qiu, T., Deis, R., Hart, N., Levy, K., Masek, M., Shawahny, A., Ahmad, A., Eitan, H., et al. (2022). Control of meiotic chromosomal bouquet and germ cell morphogenesis by the zygotene cilium. Science *376*, eabh3104. 10.1126/science.abh3104.

58. Lu, W., and Gelfand, V.I. (2017). Moonlighting Motors: Kinesin, Dynein, and Cell Polarity. Trends in Cell Biology *27*, 505-514. 10.1016/j.tcb.2017.02.005.

59. Krøvel, A.V., and Olsen, L.C. (2002). Expression of a vas::EGFP transgene in primordial germ cells of the zebrafish. Mech Dev *116*, 141-150. 10.1016/s0925-4773(02)00154-5.

60. Rapali, P., Szenes, Á., Radnai, L., Bakos, A., Pál, G., and Nyitray, L. (2011). DYNLL/LC8: a light chain subunit of the dynein motor complex and beyond. The FEBS Journal *278*, 2980-2996. https://doi.org/10.1111/j.1742-4658.2011.08254.x.

61. Cheng, S., Altmeppen, G., So, C., Welp, L.M., Penir, S., Ruhwedel, T., Menelaou, K., Harasimov, K., Stützer, A., Blayney, M., et al. (2022). Mammalian oocytes store mRNAs in a mitochondria-associated membraneless compartment. Science *378*, eabq4835. doi:10.1126/science.abq4835.

62. Insinna, C., Baye, L.M., Amsterdam, A., Besharse, J.C., and Link, B.A. (2010). Analysis of a zebrafish dync1h1 mutant reveals multiple functions for cytoplasmic dynein 1 during retinal photoreceptor development. Neural Dev *5*, 12. 10.1186/1749-8104-5-12.

63. Escobar-Aguirre, M., Zhang, H., Jamieson-Lucy, A., and Mullins, M.C. (2017). Microtubule-actin crosslinking factor 1 (Macf1) domain function in Balbiani body

dissociation and nuclear positioning. PLOS Genetics *13*, e1006983. 10.1371/journal.pgen.1006983.

64. Voorhees, P.W. (1985). The theory of Ostwald ripening. Journal of Statistical Physics *38*, 231-252. 10.1007/BF01017860.

65. Ray, S., Singh, N., Kumar, R., Patel, K., Pandey, S., Datta, D., Mahato, J., Panigrahi, R., Navalkar, A., Mehra, S., et al. (2020). α-Synuclein aggregation nucleates through liquid–liquid phase separation. Nature Chemistry *12*, 705-716. 10.1038/s41557-020-0465-9.

66. Nakashima, K.K., van Haren, M.H.I., André, A.A.M., Robu, I., and Spruijt, E. (2021). Active coacervate droplets are protocells that grow and resist Ostwald ripening. Nature Communications *12*, 3819. 10.1038/s41467-021-24111-x.

67. Zhdanov, V.P., and Kasemo, B. (1999). Nontraditional models of Ostwald ripening on solid surfaces: from physics to biology. Surface Science *437*, 307-316. https://doi.org/10.1016/S0039-6028(99)00731-1.

68. Söding, J., Zwicker, D., Sohrabi-Jahromi, S., Boehning, M., and Kirschbaum, J. (2020). Mechanisms for Active Regulation of Biomolecular Condensates. Trends in Cell Biology *30*, 4-14. 10.1016/j.tcb.2019.10.006.

69. So, M., Hall, D., and Goto, Y. (2016). Revisiting supersaturation as a factor determining amyloid fibrillation. Current Opinion in Structural Biology *36*, 32-39. https://doi.org/10.1016/j.sbi.2015.11.009.

70. Tsukita, K., Kitamata, M., Kashihara, H., Yano, T., Fujiwara, I., Day, T.F., Katsuno, T., Kim, J., Takenaga, F., Tanaka, H., et al. (2023). Phase separation of an actin nucleator by junctional microtubules regulates epithelial function. Science Advances *9*, eadf6358. doi:10.1126/sciadv.adf6358.

71. Pickering, S.U. (1907). Cxcvi. J. Chem. Soc., Trans *91*, 2001-2021.

72. Folkmann, A.W., Putnam, A., Lee, C.F., and Seydoux, G. (2021). Regulation of biomolecular condensates by interfacial protein clusters. Science *373*, 1218-1224. doi:10.1126/science.abg7071.

73. Tsukita, K., Kitamata, M., Kashihara, H., Yano, T., Fujiwara, I., Day, T.F., Katsuno, T., Kim, J., Takenaga, F., Tanaka, H., et al. (2023). Phase separation of an actin nucleator by junctional microtubules regulates epithelial function. Sci Adv *9*, eadf6358. 10.1126/sciadv.adf6358.

74. Volkov, V.A., and Akhmanova, A. Phase separation on microtubules: from droplet formation to cellular function? Trends in Cell Biology. 10.1016/j.tcb.2023.06.004.

75. Wiegand, T., and Hyman, A.A. (2020). Drops and fibers - how biomolecular condensates and cytoskeletal filaments influence each other. Emerg Top Life Sci *4*, 247-261. 10.1042/etls20190174.

76. Song, X., Yang, F., Yang, T., Wang, Y., Ding, M., Li, L., Xu, P., Liu, S., Dai, M., Chi, C., et al. (2023). Phase separation of EB1 guides microtubule plus-end dynamics. Nature Cell Biology *25*, 79-91. 10.1038/s41556-022-01033-4.

77. Ambadipudi, S., Biernat, J., Riedel, D., Mandelkow, E., and Zweckstetter, M. (2017). Liquid–liquid phase separation of the microtubule-binding repeats of the Alzheimer-related protein Tau. Nature Communications *8*, 275. 10.1038/s41467-017-00480-0.

78. Hochmair, J., Exner, C., Franck, M., Dominguez-Baquero, A., Diez, L., Brognaro, H., Kraushar, M.L., Mielke, T., Radbruch, H., Kaniyappan, S., et al. (2022). Molecular crowding and RNA synergize to promote phase separation, microtubule interaction, and

seeding of Tau condensates. The EMBO Journal *41*, e108882. https://doi.org/10.15252/embj.2021108882.

79. Chakraborty, P., and Zweckstetter, M. (2022). Phase separation of the microtubule-associated protein tau. Essays in Biochemistry *66*, 1013-1021. 10.1042/ebc20220066.

80. von Appen, A., LaJoie, D., Johnson, I.E., Trnka, M.J., Pick, S.M., Burlingame, A.L., Ullman, K.S., and Frost, A. (2020). LEM2 phase separation promotes ESCRT-mediated nuclear envelope reformation. Nature *582*, 115-118. 10.1038/s41586-020-2232-x.

81. Wang, B., Zhang, L., Dai, T., Qin, Z., Lu, H., Zhang, L., and Zhou, F. (2021). Liquid-liquid phase separation in human health and diseases. Signal Transduct Target Ther *6*, 290. 10.1038/s41392-021-00678-1.

82. Maucuer, A., Desforges, B., Joshi, V., Boca, M., Kretov, D.A., Hamon, L., Bouhss, A., Curmi, P.A., and Pastré, D. (2018). Microtubules as platforms for probing liquid–liquid phase separation in cells – application to RNA-binding proteins. Journal of Cell Science *131*. 10.1242/jcs.214692.

83. Tworzydlo, W., Kisiel, E., Jankowska, W., Witwicka, A., and Bilinski, S.M. (2016). Exclusion of dysfunctional mitochondria from Balbiani body during early oogenesis of Thermobia. Cell and Tissue Research *366*, 191-201. 10.1007/s00441-016-2414-x.

84. Kaufman, O.H., Lee, K., Martin, M., Rothhämel, S., and Marlow, F.L. (2018). rbpms2 functions in Balbiani body architecture and ovary fate. PLOS Genetics *14*, e1007489. 10.1371/journal.pgen.1007489.

85. Roovers, E.F., Kaaij, L.J.T., Redl, S., Bronkhorst, A.W., Wiebrands, K., de Jesus Domingues, A.M., Huang, H.Y., Han, C.T., Riemer, S., Dosch, R., et al. (2018). Tdrd6a

Regulates the Aggregation of Buc into Functional Subcellular Compartments that Drive Germ Cell Specification. Dev Cell *46*, 285-301.e289. 10.1016/j.devcel.2018.07.009.

86. Marlow, F.L., and Mullins, M.C. (2008). Bucky ball functions in Balbiani body assembly and animal–vegetal polarity in the oocyte and follicle cell layer in zebrafish. Developmental Biology *321*, 40-50. https://doi.org/10.1016/j.ydbio.2008.05.557.

87. Yan, W., Ma, L., Zilinski, C.A., and Matzuk, M.M. (2004). Identification and Characterization of Evolutionarily Conserved Pufferfish, Zebrafish, and Frog Orthologs of GASZ1. Biology of Reproduction *70*, 1619-1625. 10.1095/biolreprod.103.024778.

88. Ahmad, A., Bogoch, Y., Shvaizer, G., and Elkouby, Y.M. (2023). The piRNA protein Asz1 is essential for germ cell and gonad development in zebrafish and exhibits differential necessities in distinct types of RNP granules. bioRxiv, 2023.2007.2018.549483. 10.1101/2023.07.18.549483.

89. Parichy, D.M., Elizondo, M.R., Mills, M.G., Gordon, T.N., and Engeszer, R.E. (2009). Normal table of postembryonic zebrafish development: Staging by externally visible anatomy of the living fish. Developmental Dynamics *238*, 2975-3015. https://doi.org/10.1002/dvdy.22113.

90. Riemer, S., Bontems, F., Krishnakumar, P., Gömann, J., and Dosch, R. (2015). A functional Bucky ball-GFP transgene visualizes germ plasm in living zebrafish. Gene Expr Patterns *18*, 44-52. 10.1016/j.gep.2015.05.003.

91. Bontems, F., Stein, A., Marlow, F., Lyautey, J., Gupta, T., Mullins, M.C., and Dosch, R. (2009). Bucky ball organizes germ plasm assembly in zebrafish. Curr Biol *19*, 414-422. 10.1016/j.cub.2009.01.038.

92. Revenu, C., Streichan, S., Donà, E., Lecaudey, V., Hufnagel, L., and Gilmour, D. (2014). Quantitative cell polarity imaging defines leader-to-follower transitions during collective migration and the key role of microtubule-dependent adherens junction formation. Development *141*, 1282-1291. 10.1242/dev.101675.

93. Choi, H.M., Beck, V.A., and Pierce, N.A. (2014). Next-generation in situ hybridization chain reaction: higher gain, lower cost, greater durability. ACS Nano *8*, 4284-4294. 10.1021/nn405717p.

94. Mytlis, A., and Elkouby, Y.M. (2021). Live and Time-Lapse Imaging of Early Oogenesis and Meiotic Chromosomal Dynamics in Cultured Juvenile Zebrafish Ovaries. Methods Mol Biol *2218*, 137-155. 10.1007/978-1-0716-0970-5_12.

95. Sasson, E., Anzi, S., Bell, B., Yakovian, O., Zorsky, M., Deutsch, U., Engelhardt, B., Sherman, E., Vatine, G., Dzikowski, R., and Ben-Zvi, A. (2021). Nano-scale architecture of blood-brain barrier tight-junctions. eLife *10*, e63253. 10.7554/eLife.63253.

96. Goedhart, J., and Luijsterburg, M.S. (2020). VolcaNoseR is a web app for creating, exploring, labeling and sharing volcano plots. Scientific Reports *10*, 20560. 10.1038/s41598-020-76603-3.

97. Metsalu, T., and Vilo, J. (2015). ClustVis: a web tool for visualizing clustering of multivariate data using Principal Component Analysis and heatmap. Nucleic Acids Res *43*, W566-570. 10.1093/nar/gkv468.

98. Ge, S.X., Jung, D., and Yao, R. (2020). ShinyGO: a graphical gene-set enrichment tool for animals and plants. Bioinformatics *36*, 2628-2629. 10.1093/bioinformatics/btz931.

99. Consortium, T.U. (2022). UniProt: the Universal Protein Knowledgebase in 2023. Nucleic Acids Research *51*, D523-D531. 10.1093/nar/gkac1052.

100. He, B., Wang, K., Liu, Y., Xue, B., Uversky, V.N., and Dunker, A.K. (2009). Predicting intrinsic disorder in proteins: an overview. Cell Research *19*, 929-949. 10.1038/cr.2009.87.

101. Prilusky, J., Felder, C.E., Zeev-Ben-Mordehai, T., Rydberg, E.H., Man, O., Beckmann, J.S., Silman, I., and Sussman, J.L. (2005). FoldIndex©: a simple tool to predict whether a given protein sequence is intrinsically unfolded. Bioinformatics *21*, 3435-3438. 10.1093/bioinformatics/bti537.

102. Walsh, I., Martin, A.J.M., Di Domenico, T., and Tosatto, S.C.E. (2011). ESpritz: accurate and fast prediction of protein disorder. Bioinformatics *28*, 503-509. 10.1093/bioinformatics/btr682.

103. Lancaster, A.K., Nutter-Upham, A., Lindquist, S., and King, O.D. (2014). PLAAC: a web and command-line application to identify proteins with prion-like amino acid composition. Bioinformatics *30*, 2501-2502. 10.1093/bioinformatics/btu310.

Acknowledgments

We are grateful to Roland Dosch, Rene Ketting, and Karuna Sampath for the *Tg(buc:Buc-GFP)*, *Tg(vasa:GFP)*, and *Tg(bact:EMTB-3XGFP)* lines. We thank Yaron Shav-Tal for his valuable advice on the analyses of our in vivo FRAP experiments, and Reuven Vainer for his valuable advice on the Buc IP and supernatant/pellet experiments.

Funding

Israel Science Foundation – grant no. 558/19 (YME)

Author contributions

Conceptualization: RD, SK, AA, YB, YME

Methodology: RD, SK, AA, YB, AD, GS, ES, AM, ABZ, YME

Investigation: RD, SK, AA, YB, AD, GS, ES, AM

Visualization: RD, SK, ES, YME

Funding acquisition: YME

Supervision: ABZ, YME

Writing – original draft: RD, SK, AA, YME

Competing interests

The authors declare no competing interests.

Data and materials availability

Supplementary Materials

Supplementary Figures 1-14

Supplementary Movies 1-13

Supplementary Tables 1-2

Figure legends

Figure 1. Buc undergoes liquid-liquid phase-separation during early Bb formation.

A. Top: Bb formation during oocyte development, indicating oocyte stages and sizes. Bottom:

Live imaging of transgenic Buc-GFP (green, top) and antibody labeling of endogenous Buc (red, bottom) detect small granules (arrowheads) that are not localized to the main aggregate, specifically during early Bb formation, and not in later formation or in the mature Bb stages (two right panels). **B.** Live time-lapse imaging of Buc-GFP granules (green) in ovaries exhibit liquid droplet-like dynamics, showing granules that condense in real time (top), fuse with other granules (middle; orange and white arrowheads), and granules that translocate to and fuse with the main aggregates (bottom). DNA (blue) is labeled by Hoechst. Scale bars are 10 μm. Time (minutes) is indicated. Images are snapshots from Movies S1-3. **C.** Treatment of live cultured Buc-GFP (green) ovaries with 5% or 10% 1,6-Hexanediol (right panels as indicated). T_0 shows oocytes prior to treatment. Control ovaries were treated with solvent only (methanol, left panels). Each control oocyte (T_0-T_{Final}) corresponds to the oocytes in the 5% or 10% Hexanediol treated ovaries, respectively. Images of early (top) and mid Bb formation (middle), as well as mature Bb (bottom) are shown. **D.** Ovaries co-labeled for Buc (green) and *dazl* mRNA (HCR FISH, red) after 5% or 10% 1,6-Hexanediol treatment (middle and right panels, respectively), compared to control untreated ovaries (left). In all images, DNA (blue) is labeled by Hoechst (live) or DAPI (fixed) ovaries. Bright nuclei belong to somatic follicle cells, that surround oocytes. Scale bars are 10 μm.

Figure 2. Bb RNAs form insoluble complexes in a Buc dependent manner. A. Experimental design: Ovaries are dissected from Buc-GFP fish, oocytes at all Bb stages (all sizes < 100 μm in diameter) are isolated, and lysed. Oocyte lysate is centrifuged, separating a soluble supernatant fraction and a non-soluble pellet fraction. **B.** Western blot analysis shows Buc-GFP detection in the pellet, but not supernatant fraction. Addition of L-Arg to the lysis buffer shifts Buc-GFP to the supernatant fractions in a dose-dependent manner until saturation at 1.5 M. **C-H.**

Mass-spectrometry analyses of pellet and supernatant fractions from wt and *buc*$^{-/-}$ ovaries. Volcano plots (C-E) Venn diagram (E) showing enrichment of proteins specifically in the pellet over the supernatant fraction in the wt samples (C), but not in *buc*$^{-/-}$ samples (D). **F-G.** Heatmaps with hierarchical clustering of the proteins that are specifically enriched in the pellet over supernatant samples in wt, but loose enrichment in *buc*$^{-/-}$ samples (F, see also C-D), including select known Bb proteins (G). **H.** GO analyses of Buc-dependent pellet enriched proteins identifies multiple RNA biogenesis and processing processes (red highlight). **I.** Top: Top ten Buc-dependent insoluble Bb proteins that contain substantial (~65-85%) IDR sequences. Buc (~45%) and Ziwi (~20%) are shown as positive and negative IDR control proteins, respectively. Bottom: percentage of Buc-dependent insoluble Bb proteins with or without a predicted Prion-like domain (PrLD). **J.** Live detection in Buc-GFP ovaries (phenotypically wt) of presumptive amyloid β-sheets (ThT, cyan) in mature Bb (arrowheads, top), as labeled by transgenic Buc-GFP (green) and mitochondria (MitoTracker, magenta). ThT is not detected above background levels in the early Buc-GFP-positive, mitochondria-enriched forming Bb (bottom). At mature Bb stages in *buc*$^{-/-}$ ovaries, the Bb fails to form as indicated by MitoTracker, and ThT is not detected above background levels. Transgenic Buc-GFP protein is not expressed in the *buc* mutant line. Scale bars are 10 μm.

Figure 3. Buc granule dynamics and microtubule organization during Bb formation. A-E. FRAP analyses of Buc-GFP turnover in in whole ovaries, in the early forming Bb in the nuclear cleft (top) and in the mature Bb (bottom) stages. Images in A are snapshots at indicated timepoints (minutes) from representative Movies S4-5. Recovery plots (B), as well as quantification by mobile (C) and immobile (D) fraction calculations, and by intensity at last 20 frames (E) are shown. All bars are Mean ± SD. **F.** Dynamic organization of microtubules

(transgenic EMTB-GFP, green) during oocyte development at early, mid, and mature Bb stages, in fixed (top) and live (bottom) ovaries. DNA (blue) is labeled by DAPI. Scale bars are 10 μm. **G.** Co-dynamics of Buc (red) and microtubules (EMTB-GFP, green) during oocyte development at early, mid, and mature Bb stages. DNA (blue) is labeled by DAPI. Scale bars are 10 μm. **H.** STED super-resolution microscopy shows that Buc granules (red) are located immediately adjacent to microtubule cables (EMTB-GFP, green). Shown are representative Gaussian visualization images. i and ii are zoom-in images of color-coded boxes in the left panel. Scale bars are 100 nm.

Figure 4. Turnover of Buc granules in the early forming Bb requires microtubules. FRAP analyses of Buc-GFP turnover in the early forming Bb in the nuclear cleft, in whole ovaries treated with DMSO as control, compared to nocodazole (**A-E**), or colchicine (**F-J**), or taxol (**K-O**). Images (top DMOS-control, bottom drug treated ovaries) are snapshots at indicated timepoints (minutes) from representative Movies S6 (nocodazole), S7 (colchicine), and S8 (taxol). Recovery plots (B,G,L), as well as quantification by mobile (C, H, M) and immobile (D, I, N) fraction calculations, and by intensity at last 20 frames (E, J, O) are shown. All bars are Mean ± SD.

Figure 5. Turnover of Buc granules requires dynein-mediated microtubule trafficking. A-J. FRAP analyses of Buc-GFP turnover in the early forming Bb in the nuclear cleft, in whole ovaries treated with DMSO as control, compared to ciliobrevin (A-E), or to taxol and ciliobrevin (F-J). Images in A,F are snapshots at indicated timepoints (minutes) from representative Movies S9 (ciliobrevin) and S10 (taxol+ciliobrevin). Recovery plots (B, G), as well as quantification by mobile (C, H) and immobile (D, I) fraction calculations, and by

intensity at last 20 frames (E, J) are shown. All bars are Mean ± SD. **K.** Ovaries co-labeled for dynein (red), Buc (green), and DNA (DAPI, blue), show dynein localization to the nuclear cleft. Scale bar is 5 μm. **L.** Pixelwise colocalization test in oocyte nuclear cleft ROIs confirms dynein co-localization with Buc in the nuclear cleft. Pearson's R value between 0 and 1 concludes co-localization. Bars are Mean ± SD. **M-O.** Buc-GFP-IP on oocytes isolated as in Fig. 2A, followed by mass-spectrometry analysis. Volcano plots of proteins enriched specifically in Buc-GFP-IP, versus three independent controls: Control IP (no beads, M), no transgenic GFP IP (wt, N), and no Buc, free GFP-IP (vasa:GFP, O), showing specific pull down of dynein accessory subunits Dynll1 and Dynll2b, as well as known Bb proteins. **P.** Dot-blot analysis of IP experiments as in M-O. IP (left) and input (right) samples are shown. Dynein heavy chain Dync1h1 is specifically pulled down only in Buc-GFP-IP samples, and it is detected in the input of all samples. GFP is detected in Buc-GFP and vasa:GFP IP and input samples, using anti-GFP beads, but not in control beads or wt (no GFP) IP and input samples. As specificity control, β-Act is not pulled down by Buc-GFP, and it is detected in all input samples.

Figure 6. Microtubules are required for the integrity of the Buc condensate at early-mid stages of Bb formation. A. Ovaries treated live with control DMSO (left) or nocodazole (right) and then fixed and co-labeled for mAb414 and Buc (top), or for γTub and Buc (bottom) show Buc condensate disintegration upon microtubule depolymerization. DNA (blue) is labeled by DAPI. **B.** Buc phenotype distribution from the experiments in A, are plotted. Bars are Mean ± SD from independent experiments. **C.** Examples of the measuring line (arrowheads) of Buc intensity across the cleft and the forming Bb condensate, using the centrosome (γTub) as a marker for the cleft vicinity. Buc intensity plots were classified as type I (blue in E) or type II (red in E; Methods). DNA (blue) is labeled by DAPI. **D.** Plot of the rates of each curve types in

control and nocodazole treated ovaries. **E.** Pooled Buc intensity curves in DMSO control ovaries. Type I exhibited a clear intensity peak, and type II were flattened with intensity <25% of maximal Type I peak. **F.** Pooled Buc intensity curves in nocodazole treated ovaries. **G.** Comparison of type I curves from control DMSO (blue) versus nocodazole treated ovaries (purple) show that type I curves in nocodazole samples exhibit significantly dampened peaks (asterixis indicate significant *p*-values). Thus nocodazole type I curves were classified as type III. **H.** Comparison of type I and type II curves show they are highly significantly distinct. **I.** Plot of the *p*-values of the comparison in H at each line position. **J.** Representative IMARIS 3D images of entire oocytes co-labeled for Buc (green) and γTub (red). White lines indicate the distance between automatically identified surfaces of Buc entities and the centrosome in control DMSO (left) or nocodazole (right) treated ovaries. Images are snapshots from Movies S11, additional examples are provided in Movie S12. **K-N.** The number per oocyte, of granules (K), number of granules with surface area smaller than 5 μm^2 (L), number of granules with volume smaller than 5 μm^3, and the distance between granules and the centrosome (N), are plotted for control DMSO (blue) and nocodazole treated ovaries (red). All bars are Mean ± SD from independent experiments.

Figure 7. Microtubules restrict the over-growth and coarsening of the mature Bb condensate. A. Representative IMARIS 3D live-images of Buc-GFP control (top) and nocodazole treated (bottom) oocytes at T_0 (left) and T_f (right). Oocyte contour is outlined by dashed white outline. DNA (blue) is labeled by Hoechst. Scale bars are 10 μm. **B.** Zoom in images of the Buc-GFP labeled Bb in control (top) and nocodazole (bottom) oocytes in the indicated projections and over time at three timepoints along the experiment. Images in A-B are snapshots of Movie S13 (control) and S14 (nocodazole) treated oocytes. **C.** Plots of fold-change

over time in normalized Bb volume, surface area, and density, as well as of oocyte size, in DMSO control (blue) and nocodazole treated oocytes (orange). All bars are Mean ± SD from independent experiments. **D.** Multistep control by microtubules of Buc condensation and Bb formation during oocyte development. Left: Early condensing Buc granules are trafficked by dynein on microtubules to the cleft, where they fuse and form the main early Bb condensate. The localization of Buc granules and Buc turnover in the condensate are microtubule and dynein dependent. Middle: At early-mid stages, microtubules scaffold the main condensate, and are required for its integrity, likely by providing molecular crowding agents to maintain Buc at concentrations that are sufficient for its condensed state or to support granule fusion. Right: At mature Bb stages, microtubule cage the Bb and prevents its overgrowth and coarsening, likely by serving as Pickering agents.

Supplementary Figure Legends

Figure S1. Supporting information for Figure 2. A. PCA analysis of the pellet and supernatant samples from wt and *buc*$^{-/-}$ ovaries in the experiment in Fig. 2A-H. **B.** Percentage of IDR sequences for all 114 enriched proteins from which the top 10 are shown in Fig. 2I. **C-D.** GO analyses for Cellular Components (C) and Molecular Function (D) show further RNA binding and RNP Granule categories enriched in Buc dependent Bb RNA proteins. **E-G.** IDR prediction analyses for Buc (E) as a known IDR, Ziwi (F) as negative control with very little IDR, and the top 10 proteins from Fig. 2I.

Figure S2. Supporting information for Figure 2. Prediction of Prion-like Domains (PrD) in Buc (A) as a positive control with a predicted PrD, Ziwi (B) as a negative control with no PrD predicted, and in the top 10 proteins (C) from Fig. 2I.

Figure S3. Supporting information for Figure 2. Detection of presumptive amyloid b-sheets (ThT, blue, arrowheads) in the Bb in fixed wt ovaries (top) labeled for with Buc antibody (red), and the lipid dye DiOC6 (green), which detects Bb enriched mitochondria. In *buc*$^{-/-}$ ovaries (bottom) in which the Bb fails to form as evident by the loss of Buc and the loss of DiOC6 enrichment, ThT is not detected above background levels. Sale bars are 10 μm.

Figure S4. Supporting information for Figure 3. A-B. Individual Buc recovery curves of all oocytes (individual colors) in the FRAP experiments in Fig. 3B, at mature Bb (A) and early cleft (B) stages. **C.** Mitotracker labeling of live ovaries pre- and post-FRAP, in the FRAP experiments in Fig. 3B, shows viable active mitochondria after FRAP, as control for normal cell viability under our FRAP conditions. White dashed boxes indicate the bleached regions in the FRAP. Early cleft and mature Bb stages are shown. Scale bars are 10 μm. **D.** Cross-visualization of the STEAD super-resolution Gaussian images shown in Fig. 3H. Scale bars are 100 nm. N indicates the oocyte nucleus.

Figure S5. Supporting information for Figure 4. A-F. Individual Buc recovery curves of all oocytes (individual colors) in the FRAP experiments in Fig. 4, in control DMSO (A, C, E) and drug treated (B, D, F) ovaries. **G-I.** Control EMTB-GFP ovaries treated side by side to ovaries in the FRAP experiments in Fig. 4, show microtubule depolymerization upon nocodazole (G), and colchicine (H), but not taxol (I) treatments. **J-L.** Mitochondria and cell viability controls as in Fig. S4C, for FRAP experiments and nocodazole (J), and colchicine (K), but not taxol (L)

treatments. White dashed boxes indicate the bleached regions in the FRAP. All scale bars are 10 μm.

Figure S6. Supporting information for Figure 5. A-E. Individual Buc recovery curves of all oocytes (individual colors) in the FRAP experiments in Fig. 5B, G, in control DMSO (A, C) and drug treated (B, D, E) ovaries. **F-G.** Control EMTB-GFP ovaries treated side by side to ovaries in the FRAP experiments in Fig. 5, show grossly intact microtubules with no apparent depolymerization upon ciliobrevin (F), and taxol+ciliobrevin (G) treatments. **H-I.** Mitochondria and cell viability controls as in Fig. S4C, for FRAP experiments and ciliobrevin (H), and taxol+ciliobrevin (I) treatments. White dashed boxes indicate the bleached regions in the FRAP. All scale bars are 10 μm.

Figure S7. Supporting information for Figure 5. A. Western blot control for Buc-GFP-IP experiments in Fig. 5M-O. GFP proteins are not detected in either input or Buc-GFP-IP on wt samples (no transgenic GFP; left), but are detected in both input and IP samples from Buc-GFP-IP on Buc-GFP expressing ovaries (middle) and free GFP expressing ovaries (vasa:GFP; right). **B.** Raw silver-stain analysis shows detection of proteins in input samples from Buc-GFP expressing ovaries, as well as pulled down proteins from Buc-GFP-IP samples, but not in control samples (beads with no GFP nanobody). Since the Silver-stain reaction develops rapidly gel images were taken by smartphone and some shadowing reflection of the gel might be seen. **C.** Venn diagram showing comparisons between Buc-GFP-IP samples and each independent control in IP-MS experiments in Fig. 5M-O, showing 90 proteins that are specifically enriched against all controls. **D.** Heatmap and hierarchical clustering of the 90 proteins that are specifically enriched in Buc-GFP-IP samples against all three controls (left), including known Bb proteins,

and Dynll1 and Dynll2b (right). E-F. GO analyses for Biological processes (E), Cellular components (F, left) and Molecular function (F, right) identifies relevant categories, including RNA processing, RNP- P body and stress-granule assembly, and non-membrane bound organelles (highlighted in red).

Figure S8. Supporting information for Figure 5. IDR prediction analyses for Buc (A) as a known IDR, Ziwi (B) as negative control with very little IDR, and the 10 proteins with the most extensive predicted IDR from Buc-GFP-IP samples in the experiments in Fig. 5 M-O.

Figure S9. Supporting information for Figure 5. Prediction of Prion-like Domains (PrD) in Buc (A) as a positive control with a predicted PrD, Ziwi (B) as a negative control with no PrD predicted, and the 10 proteins with the strongest predicted PrD from Buc-GFP-IP samples in the experiments in Fig. 5 M-O.

Figure S10. Supporting information for Figure 5. Raw membranes for the dot-blot analyses of the Buc-GFP-IP experiment in Fig. 5P. **A.** IP samples blotted with Dync1h1 antibody. **B.** Input samples blotted with Dync1h1 antibody. **C.** IP and input samples blotted with GFP antibody. **D.** IP and input samples blotted with β–Act antibody.

Figure S11. Supporting information for Figure 6. Representative raw data for the experiments in Fig. 6C-I, using the centrosome (γTub) as a marker for the cleft vicinity, as shown in Fig. 6C. Two representative experiments are shown #1 and #2. For each experiment, raw normalized Buc intensity curves of all individual oocytes (individual colors) are shown in control DMSO (type I: A, H, type II: B, I), and nocodazole treated ovaries (type I: D, K, type II: E, L). Plots in C and J are pooled data (type I and type II) from DMSO control ovaries, and in F

and M plots are similarly pooled data from nocodazole treated ovaries, in each experiment. Plots in G and N are comparisons between type I curves from control DMSO treated ovaries and type II curves from nocodazole treated ovaries, demonstrating they are statistically different. All bars are Mean ± SD.

Figure S12. Supporting information for Figure 6. Representative raw data for the experiments in Fig. 6C-I, using the mAb414 as a marker for delineating the cleft. **A, E.** representative images of DMSO control (A) and nocodazole treated (E) ovaries labeled with mAb4141 (red), Buc (green) and DNA (DAPI, blue). The Buc intensity measuring lines are indicated by arrowheads. Scale bars are 10 μm. **B, C, F, G.** Raw normalized Buc intensity curves of all individual oocytes (individual colors) are shown in control DMSO (type I: B, type II: C), and nocodazole treated ovaries (type I: F, type II: G). **D, H.** Plots in D are pooled data (type I and type II) from DMSO control ovaries, and in H plots are similarly pooled data from nocodazole treated ovaries, in each experiment. **I.** Plots are comparisons between type I curves from control DMSO treated ovaries and type II curves from nocodazole treated ovaries, demonstrating they are statistically different. **J.** Plots are the rate of each type I and type II curves in DMSO control and nocodazole treated ovaries in this experiment. All bars are Mean ± SD.

Figure S13. Supporting information for Figure 6. A. the number per oocyte of granules with volume smaller than 1 μm^3 for DMSO control and nocodazole treated ovaries are plotted. **B.** Raw data for Fig. 6N, plotting the distance between all granules to the centrosome in each oocyte, in the DMSO control and nocodazole treated ovaries. All bars are Mean ± SD.

Figure S14. Supporting information for Figure 7. A. Representative live images of EMTB-GFP oocytes treated with DMSO control (top) and nocodazole (bottom), side by side to

the experiments in Fig. 7A-C, at the beginning (T_0) and end (T_f) of incubation, showing intact microtubules in DMSO control and their depolymerization by nocodazole. DNA (Hoechst, blue) show oocyte nuclei as well as nuclei of surrounding follicle cells. Scale bars are 10 μm. **B.** Raw data for Fig. 7C from three independent experiments (top, middle, and bottom rows). For each experiment, the pooled data per experiment are plotted for fold-change over time of Bb volume (left), surface area (middle), and density (right), in DMSO control (blue) and nocodazole treated (orange) oocytes. All bars are Mean ± SD.

Supplementary Movie Legends

Movie S1-3. Supporting Movies for Fig. 1B. Live time-lapse imaging of Buc-GFP granules (green) in ovaries exhibit liquid droplet-like dynamics, showing granules that condense in real time (Movie S1), fuse with other granules (Movie S2; orange and white arrowheads), and granules that translocate to and fuse with the main aggregates (Movie S3). DNA (blue) is labeled by Hoechst. Scale bars are 10 μm. Time (minutes) is indicated.

Movie S4-5. Supporting Movies for Figure 3. Live time-lapse imaging of FRAP analyses of Buc-GFP turnover in in whole ovaries, in the mature Bb (Movie S4) and the early forming Bb in the nuclear cleft (Movie S5). White outline indicates oocyte contour, red boxes indicate bleached FRAP area. Scale bars are 5 μm, time is indicated (seconds).

Movie S6. Supporting Movies for Figure 4. A. Live time-lapse imaging of FRAP analyses of Buc-GFP turnover in the early forming Bb in whole ovaries, treated with control DMSO (left) and nocodazole (right) . White outline indicates oocyte contour, red boxes indicate bleached FRAP area. Scale bars are 5 µm, time is indicated (seconds).

Movie S7. Supporting Movies for Figure 4. A. Live time-lapse imaging of FRAP analyses of Buc-GFP turnover in the early forming Bb in whole ovaries, treated with control DMSO (left) and colchicine (right) . White outline indicates oocyte contour, red boxes indicate bleached FRAP area. Scale bars are 5 µm, time is indicated (seconds).

Movie S8. Supporting Movies for Figure 4. A. Live time-lapse imaging of FRAP analyses of Buc-GFP turnover in the early forming Bb in whole ovaries, treated with control DMSO (left) and taxol (right) . White outline indicates oocyte contour, red boxes indicate bleached FRAP area. Scale bars are 5 µm, time is indicated (seconds).

Movie S9. Supporting Movies for Figure 5. A. Live time-lapse imaging of FRAP analyses of Buc-GFP turnover in the early forming Bb in whole ovaries, treated with control DMSO (left) and ciliobrevin (right) . White outline indicates oocyte contour, red boxes indicate bleached FRAP area. Scale bars are 5 µm, time is indicated (seconds).

Movie S10. Supporting Movies for Figure 5. A. Live time-lapse imaging of FRAP analyses of Buc-GFP turnover in the early forming Bb in whole ovaries, treated with control DMSO (left) and ciliobrevin (center), and taxol+ciliobrevin (right) . White outline indicates oocyte contour, red boxes indicate bleached FRAP area. Scale bars are 5 µm, time is indicated (seconds).

Movies S11-12. Supporting Movies for Figure 6. Representative IMARIS 3D images of entire oocytes co-labeled for Buc (green, white arrowheads) and γTub (red, yellow arrowheads), and DNA (DAPI, blue), in control DMSO (top) and nocodazole (bottom) treated ovaries. White lines indicate the distance between automatically identified surfaces of Buc entities and the centrosome, as shown on the composite images (left) and without other channels (right). Red arrowheads point to nuclei of follicle cells that surround the oocytes, and are shown from different positions through the Z axis. Movie S11 and S12 show examples of two oocytes.

Movies S13. Supporting Movies for Figure 7. Live imaging of Buc-GFP oocytes from the experiments in Fig. 7A-C. 3D IMARIS live images of entire oocytes are shown on the left, and zoom-in live images of the Buc-GFP labeled Bb are shown on the right. The movie shows oocyte and zoomed in Bb images throughout the course of the experiment from the XY projection and then from YZ and XZ projections in control DMSO treated oocytes, followed by the coresponding images and projections in nocodazole treated oocyte. DNA (blue) is labeled by Hoechst. Scale bars are 10 μm (left) and 3 μm (right).

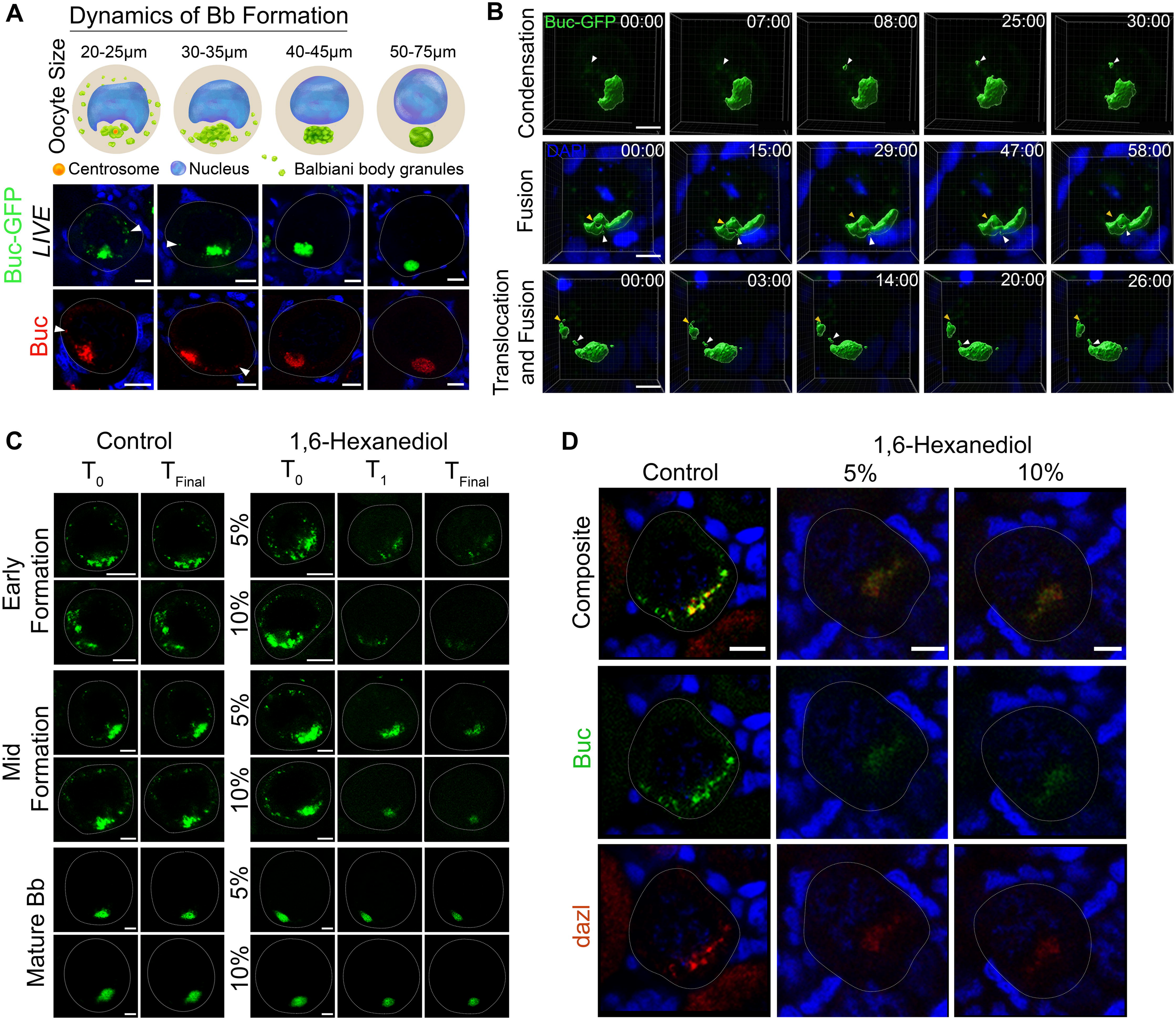
A
Dynamics of Bb Formation
Oocyte Size
20-25μm
30-35μm
40-45μm
50-75μm
Centrosome
Nucleus
Balbiani body granules
Buc-GFP
LIVE
Buc
B
Condensation
Buc-GFP
00:00
07:00
08:00
25:00
30:00
Fusion
DAPI
00:00
15:00
29:00
47:00
58:00
Translocation and Fusion
00:00
03:00
14:00
20:00
26:00
C
Control
1,6-Hexanediol
T0
TFinal
T0
T1
TFinal
Early Formation
5%
10%
Mid Formation
5%
10%
Mature Bb
5%
10%
D
1,6-Hexanediol
Control
5%
10%
Composite
Buc
dazl

A
Tg(buc:buc-gfp-buc 3'utr)
Ovary Dissection
Cell Isolation & Cell Lysis
Buc-GFP
100µm
100µm
oocytes <100µm collected
B
+L-Arginine
Supernatant
-
0.5M
1.0M
1.5M
2.0M
250kD
150
100
75
Pellet
-
0.5M
1.0M
1.5M
2.0M
250kD
150
100
75
C
Enriched Proteins wt sup vs. pellet
Significance (-Log10)
Fold Change (Log2)
igf2bp3
buc
igf2bp1
stau1
stau2
dynll2b
D
Enriched Proteins buc-/- sup vs. pellet
Significance (-Log10)
Fold Change (Log2)
stau2
dynll2b
stau1
igf2bp1
igf2bp3
buc
E
wt p>s
114
128
69
buc-/- p>s
F
wt Pellet
wt Sup
buc-/- Pellet
buc-/- Sup
G
buc
igf2bp1
stau1
stau2
igf2bp3
lsm14b
zar1
ybx1
buc-/- Pellet
buc-/- Sup
buc-/- Pellet
wt Pellet
wt Sup
H
Go Biological Processes
Chromatin assembly
Nucleosome assembly
Chromatin disassembly
Nucleosome organization
DNA packaging
Chromatin remodeling
Protein-DNA organization
Protein-DNA complex assmbly
RNA splicing via transesterfications
RNA splicing
mRNA splicing via spliceosome
DNA conformation change
RNA splicing
Chromatin organization
Ribosome biogenesis
Ribonucleoprotein complex biogenesis
mRNA processing
mRNA metabolic processes
RNA processing
Cellular comparment biogenesis
N. of Genes
20
30
40
50
-log10(FDR)
10
12
14
16
-log10(FDR)
I
Average % IDR in wt enriched proteins
Average % of IDR
si:ch211-113a14.18
acin1b
thrap3b
ybx1
eif4enif1
sfpq
lsm14ab
akap8l
lsm14aa
hnrnpabb
buc
ziwi
Number of PrLDs in wt enriched proteins
13%
87%
PrLD Present
PrLD Absent
J
ThT
Buc-GFP
MitoTracker
Composite
Mature Bb
Buc-GFP (wt)
buc-/-
Early
Buc-GFP (wt)

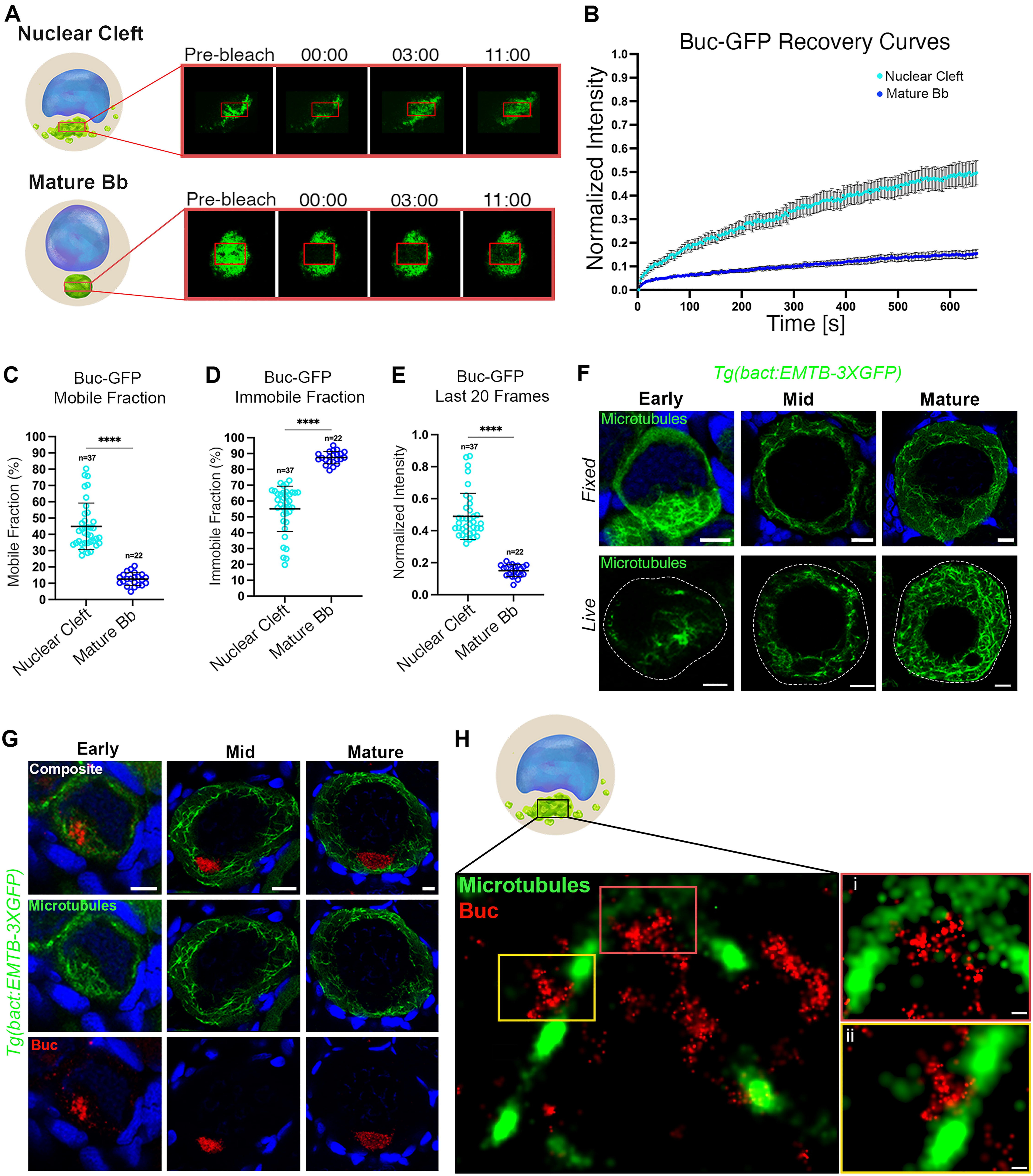
A
Nuclear Cleft
Pre-bleach
00:00
03:00
11:00
Mature Bb
Pre-bleach
00:00
03:00
11:00
B
Buc-GFP Recovery Curves
Nuclear Cleft
Mature Bb
Normalized Intensity
1.0
0.9
0.8
0.7
0.6
0.5
0.4
0.3
0.2
0.1
0.0
0
100
200
300
400
500
600
Time [s]
C
Buc-GFP Mobile Fraction
Mobile Fraction (%)
100
90
80
70
60
50
40
30
20
10
0
****
n=37
n=22
Nuclear Cleft
Mature Bb
D
Buc-GFP Immobile Fraction
Immobile Fraction (%)
100
90
80
70
60
50
40
30
20
10
0
****
n=37
n=22
Nuclear Cleft
Mature Bb
E
Buc-GFP Last 20 Frames
Normalized Intensity
1.0
0.8
0.6
0.4
0.2
0.0
****
n=37
n=22
Nuclear Cleft
Mature Bb
F
Tg(bact:EMTB-3XGFP)
Early
Mid
Mature
Fixed
Live
Microtubules
Microtubules
G
Early
Mid
Mature
Tg(bact:EMTB-3XGFP)
Composite
Microtubules
Buc
H
Microtubules
Buc
i
ii

A
DMSO (Control)
Pre-bleach
00:00
03:00
11:00
Nocodazole Treated
Pre-bleach
00:00
03:00
11:00
B
Buc-GFP Recovery Curves + Nocodazole
Nocodazole
DMSO (ctrl)
Normalized Intensity
Time [s]
C
Buc-GFP Mobile Fraction
Mobile Fraction (%)
n=20
n=17
****
Nocodazole
DMSO (ctrl)
D
Buc-GFP Immobile Fraction
Immobile Fraction (%)
n=20
n=17
****
Nocodazole
DMSO (ctrl)
E
Buc-GFP Last 20 Frames
Normalized Intensity
n=20
n=17
****
Nocodazole
DMSO (ctrl)
F
DMSO (Control)
Pre-bleach
00:00
03:00
11:00
Colchicine Treated
Pre-bleach
00:00
03:00
11:00
G
Buc-GFP Recovery Curves + Colchicine
Colchicine
DMSO (ctrl)
Normalized Intensity
Time [s]
H
Buc-GFP Mobile Fraction
Mobile Fraction (%)
n=14
n=12
****
Colchicine
DMSO (ctrl)
I
Buc-GFP Immobile Fraction
Immobile Fraction (%)
n=14
n=12
****
Colchicine
DMSO (ctrl)
J
Buc-GFP Last 20 Frames
Normalized Intensity
n=14
n=12
****
Colchicine
DMSO (ctrl)
K
DMSO (Control)
Pre-bleach
00:00
03:00
11:00
Taxol Treated
Pre-bleach
00:00
03:00
11:00
L
Buc-GFP Recovery Curves + Taxol
Taxol
DMSO (ctrl)
Normalized Intensity
Time [s]
M
Buc-GFP Mobile Fraction
Mobile Fraction (%)
n=17
n=14
ns
Taxol
DMSO (ctrl)
N
Buc-GFP Immobile Fraction
Immobile Fraction (%)
n=17
n=14
ns
Taxol
DMSO (ctrl)
O
Buc-GFP Last 20 Frames
Normalized Intensity
n=17
n=14
**
Taxol
DMSO (ctrl)

A
DMSO (Control)
Ciliobrevin Treated
Pre-bleach
00:00
03:00
11:00
B
Buc-GFP Recovery curves + Ciliobrevin D
Normalized Intensity
Time [s]
C
Buc-GFP Mobile Fraction
Mobile Fraction (%)
n=20
n=15
****
Ciliobrevin D
DMSO (ctrl)
D
Buc-GFP Immobile Fraction
Immobile Fraction (%)
E
Buc-GFP Last 20 Frames
Normalized Intensity
F
DMSO (Control)
Ciliobrevin D +Taxol Treated
G
Buc-GFP Recovery curves Taxol + Ciliobrevin D
H
Buc-GFP Mobile Fraction
n=15
n=12
n=10
Taxol + Ciliobrevin D
DMSO (ctrl)
Taxol
I
Buc-GFP Immobile Fraction
J
Buc-GFP Last 20 Frames
K
Merge
Dynein + Buc
Dynein
Buc
L
Pixelwise Colocalization with Dynein
Pearson's R Value
n=34
M
Enrichment of Proteins Buc-GFP IP vs Control IP
Proteins Enriched in Control IP
Proteins Enriched in Buc-GFP IP
buc
igf2bp3
stau2
dynll2b
dynll1
stau1
igf2bp1
Significance (-Log10)
Fold Change (Log2)
N
Enrichment of Proteins Buc-GFP IP vs wt IP
Proteins Enriched in wt IP
Proteins Enriched in Buc-GFP IP
O
Enrichment of Proteins Buc-GFP IP vs Free GFP(vasa:GFP) IP
Proteins Enriched in Free GFP IP
Proteins Enriched in Buc-GFP IP
P
wt
Tg(buc: buc-GFP)
Tg(vasa: GFP)
IP: GFP + + - +
IP: Control beads - - + -
Blot:
αDync1h1
αGFP
α β-Act
Input:

A
DMSO (Control)
Nocodazole
BUC mab414 DAPI
BUC γ-Tubulin DAPI
B
Distibution of Buc condensate phenotypes
n=126 n=163
% of oocyte
100
75
50
25
0
Disintegrated
Normal
DMSO
Nocodazole
C
BUC mab414 DAPI
BUC γ-Tubulin DAPI
1
9
D
Distribution of normalized Buc intensity curve types
n=87 n=112
% of oocytes
100
75
50
25
0
Type I
Type II
Control
Nocodazole
E
Buc-GFP intensity curves in control ovaries
Normalized Buc intensity
8000
0
Type I
Type II
Line plot (μm)
0
2
4
6
8
F
Buc-GFP intensity curves in nocodazole treated ovaries
Normalized Buc intensity
Type III
Type II
****
***
**
*
Line plot (μm)
G
Comparison between type I and type III curves
Normalized Buc intensity
Type I (control)
Type III (noco.)
****
***
**
*
Line plot (μm)
H
Comparison between type I and type II curves
Normalized Buc intensity
Type I (control)
Type II (noco.)
****
***
**
*
Line plot (μm)
I
P-values of the comparison in H
P-values
1.00
0.05
0.00
Line plot (μm)
0
1
2
3
4
5
6
7
8
9
J
DMSO (control)
Nocodazole
Buc
γ-tubulin
K
Total number of aggregates per oocyte
# of aggregates per oocyte
**
n=14
n=16
Control
Nocodazole
L
Number of small agregates by surface area
Number of aggregates <5um² per oocyte
**
n=14
n=16
Control
Nocodazole
M
Number of small aggregate by volume
Number of aggregates <5um³ per oocyte
**
n=14
n=16
Control
Nocodazole
N
Distance of aggregates from the centrosome
Avg. distance from centrosome per oocyte
****
n=14
n=16
DMSO
Nocodazole

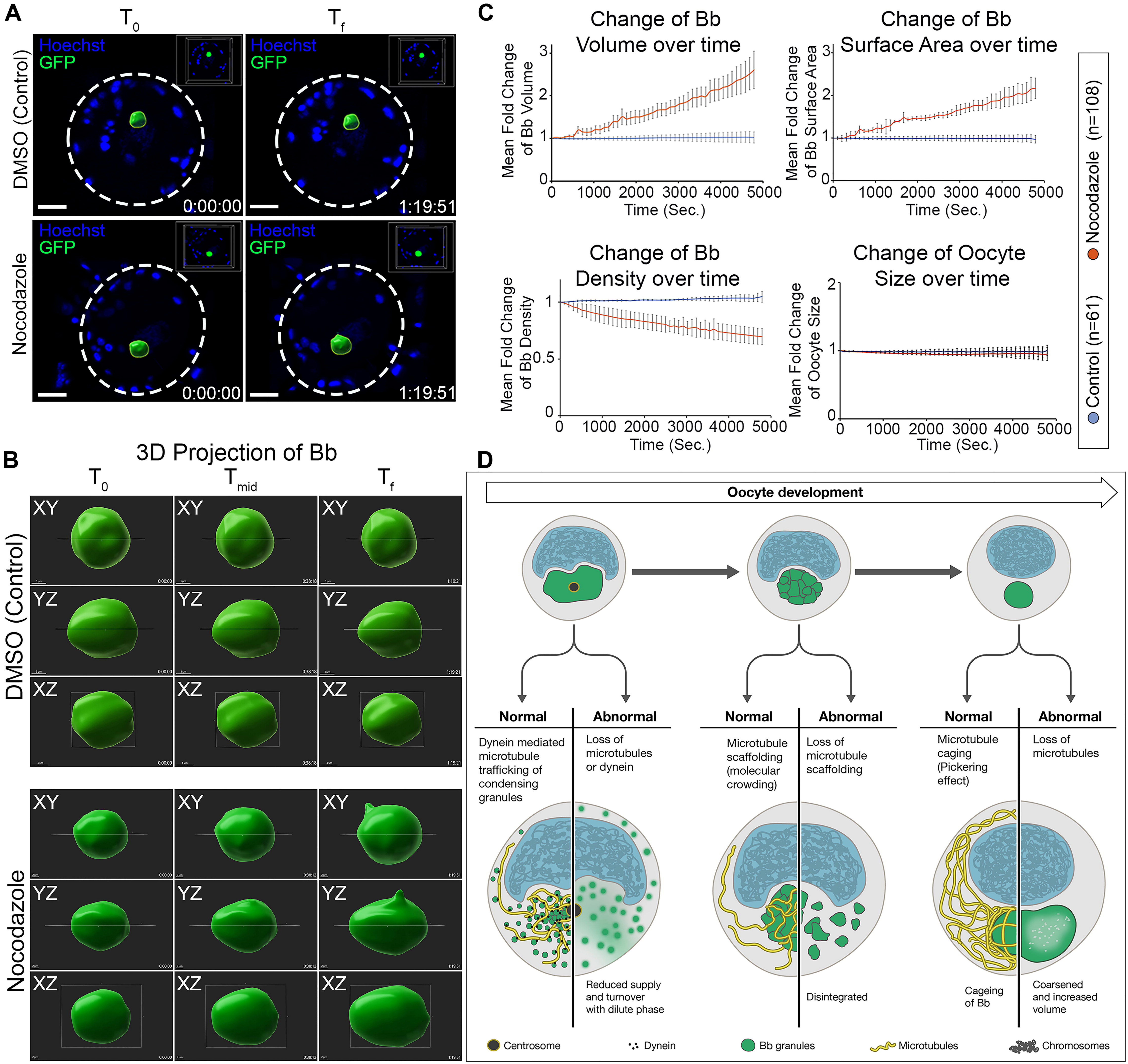
A
T0
Tf
DMSO (Control)
Nocodazole
Hoechst
GFP
0:00:00
1:19:51
B
3D Projection of Bb
T0
Tmid
Tf
DMSO (Control)
Nocodazole
XY
YZ
XZ
0:00:00
0:38:18
1:19:21
0:38:12
1:19:51
C
Change of Bb Volume over time
Mean Fold Change of Bb Volume
Change of Bb Surface Area over time
Mean Fold Change of Bb Surface Area
Change of Bb Density over time
Mean Fold Change of Bb Density
Change of Oocyte Size over time
Mean Fold Change of Oocyte Size
0
0.5
1
2
3
0
1000
2000
3000
4000
5000
Time (Sec.)
● Control (n=61)
● Nocodazole (n=108)
D
Oocyte development
Normal
Abnormal
Dynein mediated microtubule trafficking of condensing granules
Loss of microtubules or dynein
Reduced supply and turnover with dilute phase
Microtubule scaffolding (molecular crowding)
Loss of microtubule scaffolding
Disintegrated
Microtubule caging (Pickering effect)
Loss of microtubules
Caging of Bb
Coarsened and increased volume
Centrosome
Dynein
Bb granules
Microtubules
Chromosomes